From outcrop to Ground Penetrating Radar images with Point-Spread Function based convolution modelling

Øystein Haugen Ødegård

Master Thesis in Reservoir Geophysics

Department of Earth Science

University of Bergen

January 15, 2021

From outcrop to Ground Penetrating Radar images with Point-Spread Function based convolution modelling

Øystein Haugen Ødegård

Abstract

Synthetic GPR data has been generated by the Point Spread Function (PSF)-based convolution modelling method. Real GPR profiles gathered on the Wordiekammen Plateau in Billefjorden, Svalbard, and at the ruins of Lyse Abbey outside Bergen, have been used as a comparison in order to validate the results. All modelling results presented here were generated using software intended for seismic modelling, and a scaling of the relevant parameters has been performed in order to run the processes. Comparison of synthetic and real data shows that using this method to generate Pre-Stack Depth-Migrated (PSDM) GPR data is possible. Using the PSF method for this purpose is a novel approach, and further testing of its use in GPR modelling is suggested.

Acknowledgements

First of all, i would like to thank my supervisor Isabelle Lecomte. She has been of great help these last couple of years, giving great insight into the world of GPR. From everything to leading the fieldwork at Lyse to providing great resources for my thesis, her help has been magnificent, and i could not have completed this work without her.

I would also like to thank my co-supervisors, Maksim Bano and Walter Wheeler. Their help has been much appreciated.

Thanks to the following license providers: NORCE, for the academic license of the software LIME NORSAR Innovation, for the use of the academic license of the NORSAR Software Suite/SeisRoX. MathWorks, for the academic license to MATLAB.

My family and friends have provided great support throughout. Especially in making 2020, a year drastically changed by the coronavirus, pass by a little easier.

Finally, i would like to thank my fellow geoscience students at UiB for a memorable time. Especially fellow student of the GPR world, Emil Lie Hansen.

Contents

List of Figures

List of Tables

Chapter 1

Introduction

1.1 Motivation

Seismic modelling by convolution applied to geomodels built from stratigraphic interpretation of outcrops is an established practice, with the aim of gaining a better understanding of seismic images. The present work is a study of one of the convolution methods used in seismic, and extend this method to simulate Ground Penetrating Radar (GPR) data. Even though GPR is a geophysical method using electromagnetic (EM) waves instead of elastic waves in seismic, the two methods are based on similar principles. GPR may indeed benefit from modelling approaches developed from seismic imaging. In order to validate the method, the modelled images are compared to real data gathered at various outcrops at different scales.

The modelling method used in this study, PSF-based convolution is explained in section 2.1. The main benefit of this method is a reduced calculation time compared to full waveform approaches, such as finite difference (FD) modelling. Another potential benefit, is that the PSF-based convolution directly produces PSDM results. Though GPR data are not routinely depth-migrated, simulating PSDM images may help better relate the synthetic data to the observed geology at an outcrop, and provide an understanding of what GPR surveys can and cannot image. Other modelling methods are also available, such as ray-tracing, which can be used to produce synthetic radargrams (Goodman, 1994), though they don't offer the same flexibility in terms of model details.

The data presented here include large scale models with depth in the tens of meters, and smaller scale models with depth as low as below 1 m. The large scale models are based on outcrops and GPR data from Wordiekammen in Billefjorden on Svalbard. This location is interesting because of its paleokarst features (Janocha et al., 2020) (Tveranger et al., 2020). Smaller scale models were based not on geological outcrops, but on semi-restaurated walls at the Lyse site in Bergen. The advantage of

this data is that a much closer inspection of the conditions and features were available. Although these small scale outcrop-equivalents are not particularly related to the large scale limestone outcrops, they serve as a valuable control of the method in practice.

Increased knowledge on the use of PSF-based convolution modelling of GPR data can help provide an alternative to FD-modelling for such data. And as an already efficient modelling method of seismic data, it can help bridge the gap between the two geophysical methods.

1.2 Theoretical background

:

The basic principle in GPR surveys is the same as reflection seismics, as interfaces between media of different properties result in a portion of the wave energy being reflected. An EM pulse is transmitted from a source antenna, and a response of incoming reflected signals are received at a receiver antenna. For practical reasons, the GPR method is usually performed as common-offset surveys, as the distance from source to receiver is constant. The two antennas are usually separated by a distance below one wavelength, and the aquisition can be viewed as zero-offset. The propagation of EM waves can be described by the Maxwell Equations:

$$\nabla \times \vec{H} = \vec{J}_T = \sigma \vec{E} + \epsilon \frac{\partial \vec{E}}{\partial t} \tag{1.1}$$

$$\nabla \times \vec{E} = \frac{\partial \vec{B}}{\partial t} = -\mu_0 \frac{\partial \vec{H}}{\partial t} \tag{1.2}$$

$$\nabla \cdot \vec{D} = \rho \tag{1.3}$$

$$\nabla \cdot \vec{B} = 0 \tag{1.4}$$

These equations, Ampere's Law for changing electric fields (1.1), Faraday's Law of induction (1.2), Gauss' Law (1.3),and the relation that states that there are no magnetic monopoles (1.4), can be combined to form the equation of EM field propagation (Guéguen and Palciauskas, 1994):

TABLE 1.1: The properties used in equations 1.1 - 1.5

Symbol	Property
E	Electric field intensity
D	Electric displacement
H	Magnetic field intensity
B	Magnetic flux density
σ	Electric conductivity
ε	Dielectric permittivity
μ_0	Magnetic permeability of free space

$$\nabla^2 \vec{E} = \sigma \mu_0 \frac{\partial \vec{E}}{\partial t} + \epsilon \mu_0 \frac{\partial^2 \vec{E}}{\partial t^2} \tag{1.5}$$

The two most important physical parameters for a medium in regards to GPR is dielectric permittivity, ε, and electrical conductivity, σ. Dielectric permitivity is a complex value, but for the purposes of this study its imaginary component will be ignored. In addition dielectric permittivity as a value is easier to handle in this context as a relative value, i.e. its dielectric constant,κ. For any material, its dielectric constant is defined as its real-value permittivity, ϵ_r (with unit F/m), divided by the real-valued permittivity of free space ϵ_0:

$$\kappa = \frac{\epsilon_r}{\epsilon_0} \tag{1.6}$$

The permittivity of free space $\epsilon_0 = 8.854 * 10^{-11} F/m$ is approximately equal to that of air, and is the lowest possible value for this parameter.

The conductivity of the medium should ideally be low in order to obtain good GPR-results. The higher the conductivity of a material, the faster electromagnetic energy is dissipated. Soils with high water content for example have a high conductivity and attenuation leading to low wave penetration. On the contrary, dry or frozen grounds, or even ice, are better suited for GPR surveying, because of their low electrical conductivity. In addition to these, magnetic permeability is also a parameter with an effect on electromagnetic wave propagation, but it is often negligible. The conductivity and dielectric constant of some selected materials are shown in table 1.2

The parameters described above determine the velocity and attenuation of a propagating electromagnetic wave. The following formula, with c being the speed of light,

gives electromagnetic velocity, assuming that the magnetic permeability is negligible (which it is assumed to be for all models and profiles in this study):

$$v = \frac{c}{\sqrt{\kappa}} \tag{1.7}$$

The greater the contrast in permittivity at an interface, the higher the reflection coefficient. In seismic, the reflection coefficient at zero offset (R_0) is reliant on the acoustic impedance of the media involved, i.e. product of velocity and density. For GPR, the equivalent property is the EM-wave impedance, Z, which relies only on the dielectric constant of the media (for high frequencies, and assuming negligible magnetic permeability) (Annan, 2009). The formula for EM-wave impedance 1.8 is given below ($Z_0 = 377\Omega$, is the impedance of free space). The reflection coefficient of transverse electric (TE)-waves is given in formula 1.9 (with θ_1 and θ_2 being the incidence and transmitted angles, respectively). This reflection coefficient, as well as propagation of TE-waves, has been shown to be analogous to the reflection of acoustic waves (Laurain and Lecomte, 2001).

$$Z = \frac{Z_0}{\sqrt{\kappa}} \tag{1.8}$$

$$R_{TE} = \frac{\frac{1}{Z_1}\theta_1 - \frac{1}{Z_2}\theta_2}{\frac{1}{Z_1}\theta_1 + \frac{1}{Z_2}\theta_2} \tag{1.9}$$

Because of the potentially large variation in dielectric constants from material to material, a GPR survey can come across reflection coefficients much larger than one would expect to find in a seismic survey. Table 1.2 shows that the relevant geophysical parameters for GPR are strongly affected by the presence of water, and water content often increases with depth. As a result velocities tend to decrease with depth, contrary to what is common in seismics. This implications of the negative velocity trend is discussed in section 3.3.

GPR surveys do not provide the same penetration depth as seismic surveys, as the waves are attenuated faster. Just like in seismic, there is also a tradeoff between resolution and penetration. The results presented here are of a range of scales, but even greater and smaller scales are available with the GPR method (Ai et al., 2014) (Apel and Dezelic, 2005).

TABLE 1.2: Dielectric constant and electric conductivity of selected materials (from (Cassidy, 2009))

Material	Conductivity (mS/m)	Dielectric Constant
Air	0	1
Freshwater	1-10	78-88
Freshwater Ice	0.000001-1	3
Seawater	4000	81-88
Permafrost	0.1-10	2-8
Concrete (dry)	1-10	4-10
Concrete (wet)	10-100	10-20
Limestone (dry)	0.001-0.0000001	4-8
Limestone (wet)	10-100	6-15
Granite (dry)	0.001-0.00001	5-8
Sandstone (dry)	0.001-0.0000001	4-7
Sandstone (wet)	0.1-10	5-15
Soil (average)	5	16

1.3 Sites

1.3.1 Wordiekammen

The large scale data used in this study were collected at the Wordiekammen Plateau on Svalbard as part of a study on paleokarst structures in the Minkinfjellet and Wordiekammen formations (Dalsegg, Elvebakk, and Rønning, 2005). Figure 1.3 shows the location of the outcrop relevant to this study. The outcrop consists of micritic limestone layers of the Wordiekammen formation, and lies on top of the Minkinfjellet Formation. This thesis will not include any in-depth discussion of geology or a geological interpretation of these formations, and i refer to the above-mentioned reference for more information. The relevant structures are the beds, and how they form reflecting interfaces, and the visible potential collapse structure in the outcrop. A recent study on a nearby outcrop to the southwest, comprised of the Minkinfjellet and Wordiekammen formations, concluded that some features visible in outcrops extend as much as 150 meters beyond it in terms of being detected by GPR (Janocha et al., 2020). The GPR line shown in 1.3 as a red line is much closer to the outcrop than this, but this does not necessarily mean that outcropping features are easily detected by GPR in this location. Description of the data collection and model building basis for this site is found in sections 2.4.1 and 2.3.

FIGURE 1.1: Location of the Wordiekammen outcrop on Svalbard. (Image from Google Earth, accessed on 15.1.2020)

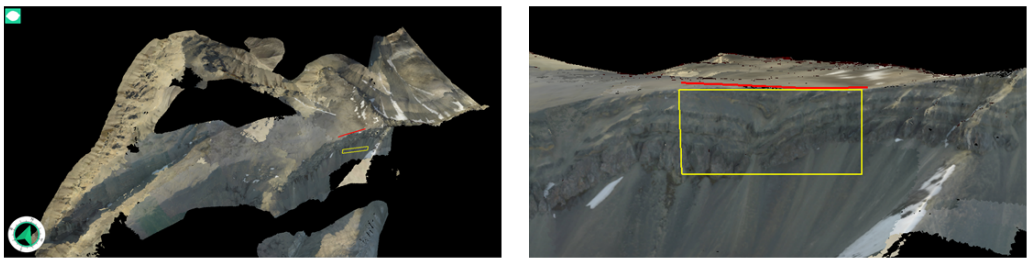

FIGURE 1.2: Overview of the Wordiekammen virtual outcrop, and the part of the outcrop used to build velocity models in this study. The red line is from a GPR profile, its length is approximately 200 m).

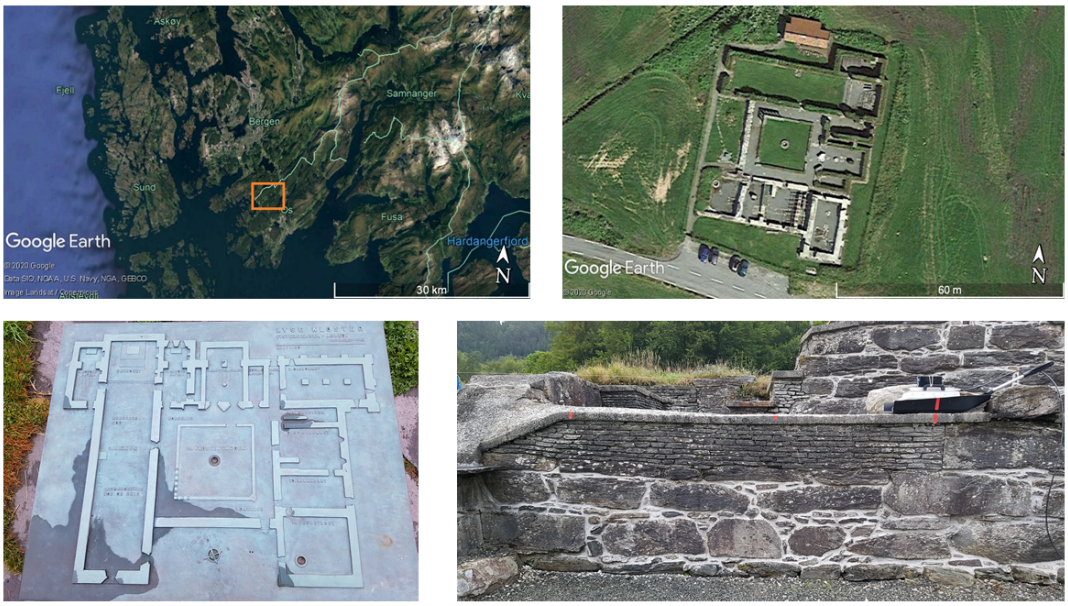

FIGURE 1.3: Location of the Lyse site, the layout of the abbey ruins, and an example of one of the walls studied. (Two upper images from Google Earth, accessed on 15.1.2020)

1.3.2 Lyse

The Lyse site consists of the ruins of a 12th century Cistercian Abbey located in Bjørnafjorden outside Bergen. The original abbey was built in soapstone from a local quarry. By the 20th century, little remained of the original structure and it was partially restored with the intention of displaying the original division of rooms and sections. This restauration was done in some places by rebuilding the base of the walls using original soapstone and modern day bricks, topped with a layer of concrete. This site still has archeological value as the area around it is thought to contain buried structures or relics/items from its origin (Hagen, 2012). Description of the data collection and model building basis for this site is found in sections 2.4.1 and 2.3.

Chapter 2

Method

2.1 PSF-based convolution

The essential principle of a simple convolution modelling method is described by formula 2.1 and figure 2.1. The medium which the signal travels through is treated as a filter, or a function of varying reflectivity. And the result observed at the source is viewed as a convolution of the pulse and that function. In one dimension (1D) this approach is very simple and the result is a trace similar to that one would expect in both seismic and GPR. Formula 2.1, shows the convolution, where P is the pulse, R the reflectivity series, and T the resulting trace. For a two-dimensional case, one could in the most simplistic sense iterate the 1D method several times across a profile. However, such a simplistic approach, will result in an overly simplistic synthetic seismic image. An example of repeated 1D-convolution is shown in figure 3.9.

$$P(t) \circledast R(t) = T(t) \tag{2.1}$$

An example of this method is shown in figures 2.2, 2.3, 2.4, which shows a PSF, a reflectivity model, and the resulting GPR image arising from the two.

In order to create an image of the subsurface, relating to the relevant reflectivity model, one will ideally want to illuminate all features present. In practice, this is not possible, and one of the issues lies especially in being able to illuminate dipping reflectors. For instance in figure 2.4 the steepest reflectors will not show in the modelled image. The reason for this is that the maximum angle of illumination was set to 25°. The method described here takes into account the fact that convolution with a two-dimensional (2D) operator, in this instance the PSF, is needed to produce 2D imaging. For this purpose, the 2D PSF takes the role of the 1D pulse. An example of a PSF is shown in figure 2.2. This PSF is a 2D-operator arising from the pulse shown

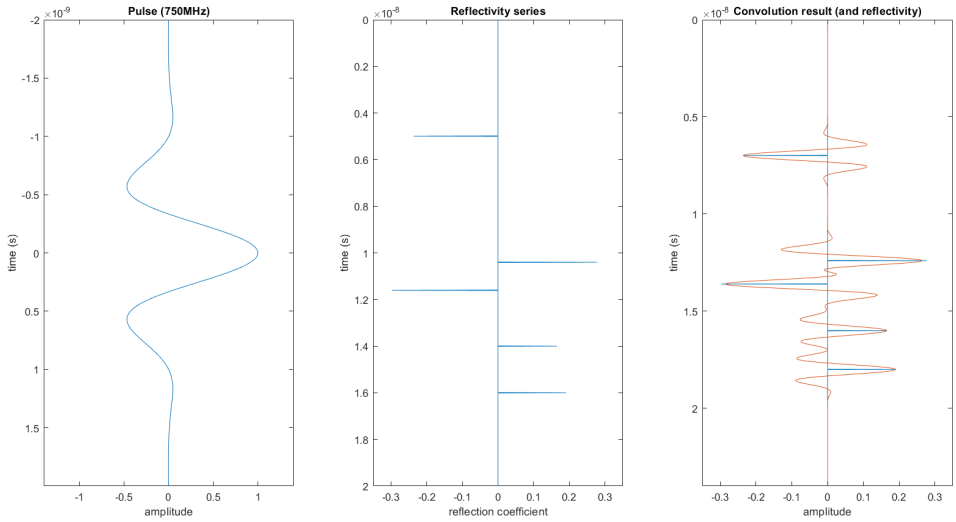

FIGURE 2.1: 1D illustration of the convolution method. Here, a 750MHz Gaussian pulse with 100% fractional bandwidth (left) is convolved with a reflectivity series (middle) to produce a synthetic GPR trace (right).

in figure 2.1 (a), a given mean velocity, and a maximum angle of illumination of 25°. Note that while the pulse is in time domain, the PSF is given in depth. From this 2D function we can read information about the resolution a certain modelling input will return. More information about this method in practice for seismic modelling can be found in (Andersen, 2020) (Hagevold, 2019).

The following aspects are where the application of this method differs from seismic to GPR: The vast difference in scales of parameters such as frequency, which is taken into account by the scaling in table 2.1 and the difficulty of a narrower illumination pattern, described in section 2.1.2.

Noise effects can also be simulated with the same method. The principle is the same, as a pulse is convolved over a densely populated reflectivity series consisting of randomised values, such as white noise. For 1D this described by equation 2.2, where NR is reflectivity trace simulating noise (densely and randomly populated), and NT is the resulting noisy trace. The synthetic noise result can then be included in the same plot as the convolution of the reflectivity. In this study, the noisy reflectivity, which is to be convolved with the PSF operator, is not treated same way as the ordinary reflectivity models. This is described in section 2.3.

$$P(t) \circledast NR(t) = NT(t) \tag{2.2}$$

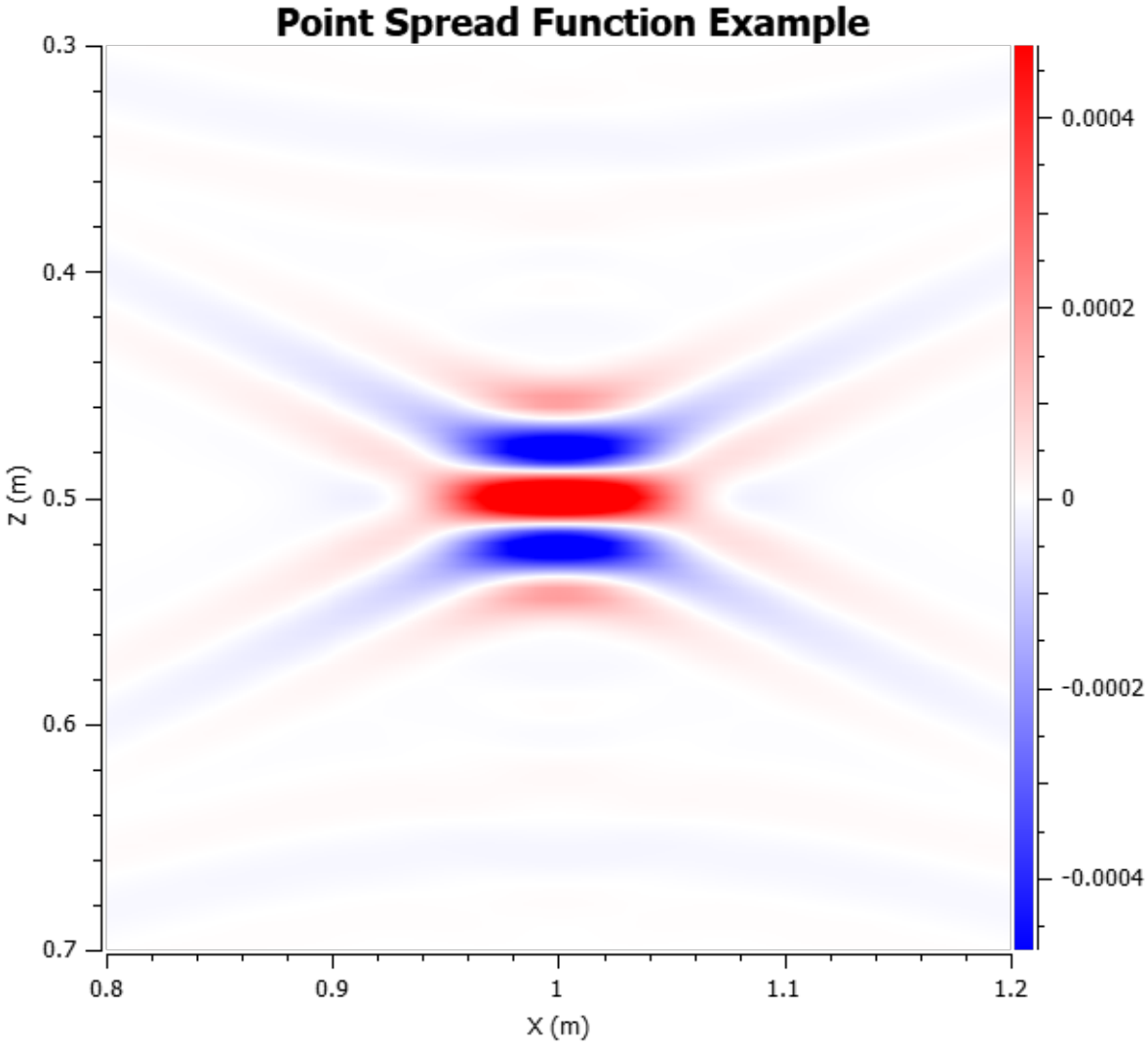

FIGURE 2.2: Example of a Point Spread Function. This function is a description of how the modelling input will treat a single point reflector. This PSF is the result of the pulse in figure 2.1 and an illumination angle of 25 degrees.

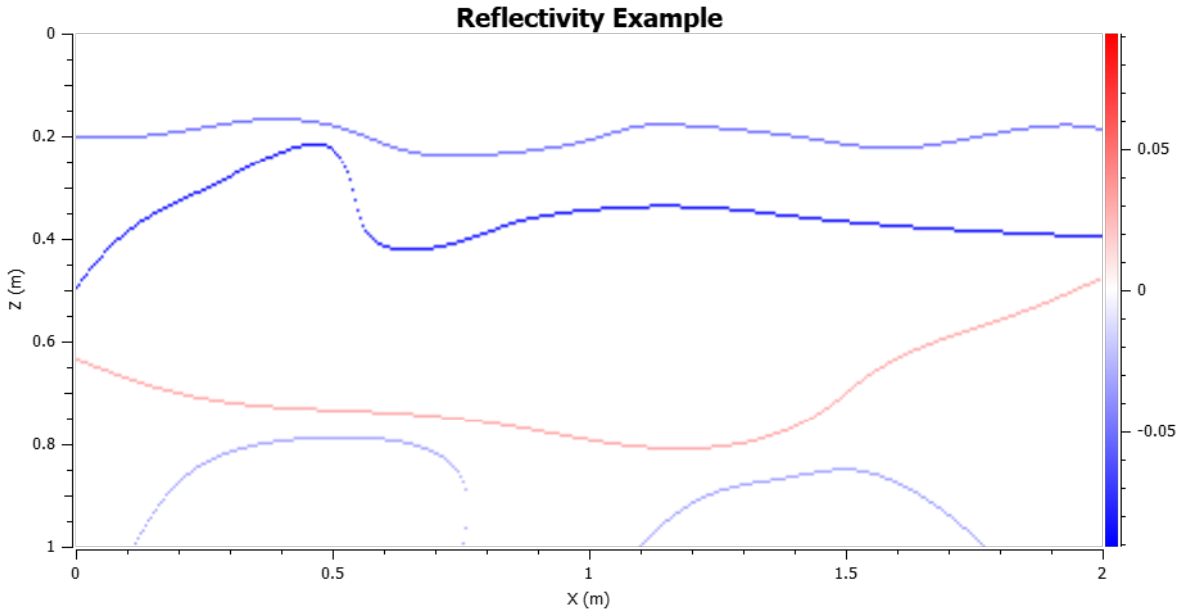

FIGURE 2.3: An example of a 2D Reflectivity model

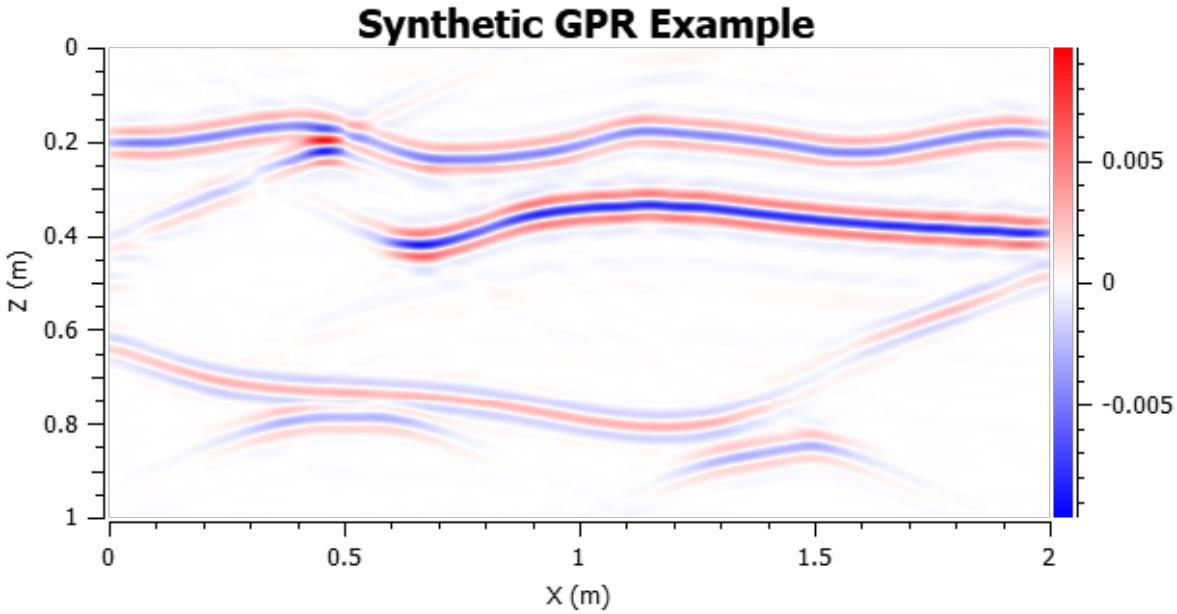

FIGURE 2.4: Example of a 2D-Result of the convolution modelling method. Based on the PSF in figure 2.2 and reflectivity in figure 2.3.

TABLE 2.1: This table shows the upscaling of EM properties to seismic equivalents in order to run modelling as if it was seismic data

Property	EM-value (actual)	Seismic value (equivalent)
Velocity	0.1m/ns	1km/s
Frequency	100MHz	1Hz
Wavelength	1m	1km
Dimensions	1m	1km

The basis for the synthetic results generated with PSF-based convolution in this study are velocity models. The complete velocity models each yield a respective reflectivity model. A pulse, preferrably resembling the relevant waveform and frequency, is used as input, together with the reflectivity series and some optional modelling parameters. Which results in a synthetic seismic profile, with correct amplitudes, and depth corresponding to that of a depth-migrated real profile. In this study, the method will be used to model GPR-data rather than seismic.

In order to run this process for GPR, the models and all pulses were upscaled to values closer to what one would expect in a seismic survey. This was necessary in order to run the modelling process in the NORSAR software. This conversion was done based on the following scheme (I.Lecomte, personal communication, 2020):

This equivalence is used to give an easier relation between the worlds of GPR and seismic, in terms of the key values frequency, velocity and wavelength. The conversion means that, for example, a 750 MHz GPR source pulse in a medium of EM wave velocity 0.1 m/ns is swapped for a 7.5 Hz pulse in a medium of P-wave velocity 1 km/s. The wavelength which then satisfies equation 2.3, approximately 0.13 km, will then perceive the seismic media in the same way an EM-wave of approximate wavelength 0.13m perceives the equivalent EM medium. The validity of this scaling is further backed up by the similarity of vertical resolution shown in the modelled and real results. Other conversions could also have been chosen as long as they satisfied equation 2.3, but the one in 2.1 is the most appropriate for this purpose.

$$\lambda = \frac{v}{f} \tag{2.3}$$

2.1.1 Wavelets

The GPR method, like seismic, relies on a source signal. When a pulse is convolved over a reflectivity series, the result is dependent on the form of that pulse. If one wanted to produce an image that resembles the actual earth as closely as possible,

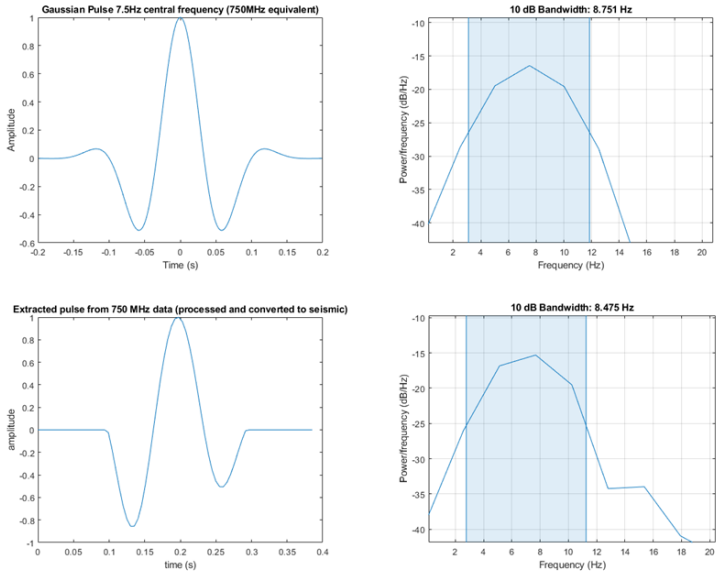

FIGURE 2.5: The high frequency pulses used, and their frequency content.

one would want the pulse to take the form of a spike, and the convolution to essentially reproduce the reflectivity as the result. Real pulses from surveys, both seismic and GPR, are not spikes. They take varying forms, and can be described by their amplitude, length, center frequency, and bandwidth.

The Ricker wavelet is often used for seismic modelling, but other waveforms are also used (Ryan, 1994). For GPR, there are also several alternatives, many of the same ones used in seismic. In this study, a synthetic gaussian pulse will be used for the modelling. These are easy to generate in MATLAB with control over their center frequency and fractional bandwidths. The Gaussian pulse is also related to the Ricker pulse, in fact a second order Gaussian with reversed polarity is equal to a Ricker wavelet.

The results of the convolution are also dependent on the frequency content of these wavelets. Both the center frequency and the bandwidth determine the result. Just like in seismic, higher frequency yields higher resolution. And a higher bandwidth, giving a shorter pulse in time, also increases resolution. The bandwidth can be described as a relative value, shown in equation 2.4, where R is tha fractional bandwidth, B is the absolute value of the bandwidth (for some loss treshold) and f_c is the center frequency (Annan, 2009).

Equations 2.5 and 2.6 show the radial and lateral resolutions of EM-waves. With v

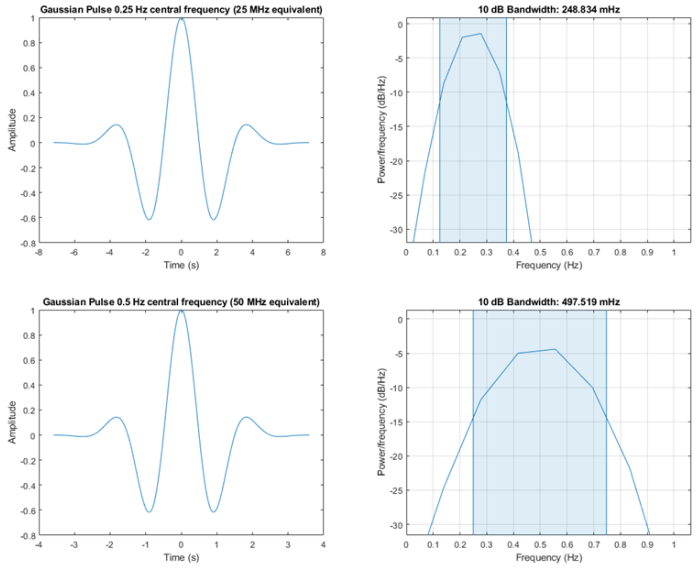

FIGURE 2.6: The low frequency pulses used, and their frequency content.

being the waves velocity, W the half-width (width at half of max amplitude), and d the distance travelled (Annan, 2009). For the calculations of vertical and horizontal resolutions shown in figure 3.1, these formulas have been used, along with the assumption that the halfwidth is equal to the inverse of the center frequency, which is not always the case in reality.

$$R = \frac{B}{f_c} \tag{2.4}$$

$$\Delta r = \frac{Wv}{4} \tag{2.5}$$

$$\Delta l = \sqrt{\frac{vdW}{2}} \tag{2.6}$$

It is also posible to extract an electromagnetic pulse-signal from a real GPR survey. If a clear and isolated reflection is available, taking such a signal from this reflection should be a good approximation of the real transmitted pulse. This has been done for the 750MHz data collected at Lyse. The wavelet and frequency content of this signal is shown in figure 2.5. The reason for extracting a reflected signal, instead of

the direct wave, is that the energy transmitted from the GPR antenna is not necessarily equally distributed in all directions. The pulse travelling horizontally directly to the receiving antenna may not have the appropriate frequency content or form.

2.1.2 Illumination pattern

In most cases concerning seismic surveys, the wave velocity increases with depth. In GPR surveys however, the opposite is true. With increasing depth, the relative dielectric permittivity also increases, which causes the electromagnetic wave velocity to drop according to 1.7.

This effect causes the angles of transmitted waves to gradually approach zero, Which again leads to a more narrow pattern of illumination than one commonly experiences in seismic surveys. A demonstration of seismic illumination patterns is shown in (Eide et al., 2018). For GPR surveys, the initial air-to-solid transition is especially problematic, as is shown in figures 2.7 and 2.8. These figures show how waves propagate upwards from a source through a velocity model with typical EM-wave velocities (given in m/ns). Figure 2.9, on the other hand, shows the propagation paths of acoustic waves upwards from a source through a seismic velocity model (velocities in km/s).

This decreasing velocity trend, and the narrow illumination effect that follows is particularly important to take into consideration when performing convolution modelling of GPR data. As the maximum take off angle from the source, which is equal to the maximum dip angle is an important parameter entered in to the calculation of the synthetic data (this is further discussed in section **??**sec:illumsec), and the angles calculated here are based on a velocity model like the one in figure 2.7). This angle is significantly reduced in comparison to a seismic model, mostly due to the air-to-solid transition. The decrease of this angle, causes a worsening of lateral resolution, because features consisting of dipping reflectors over a certain angle (the maximum dip-angle) will not be captured.

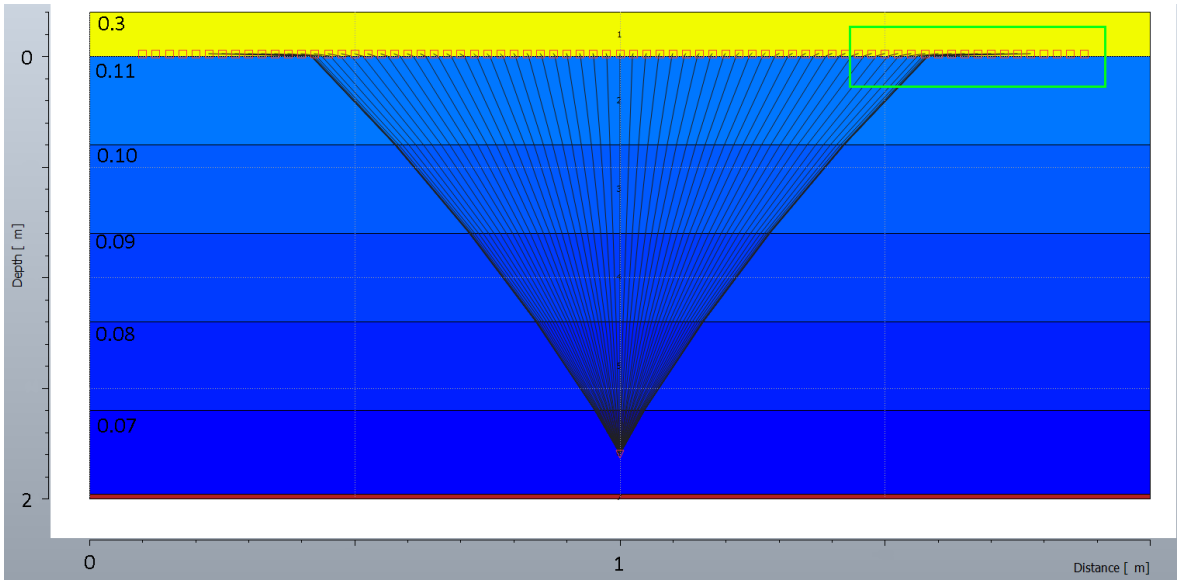

FIGURE 2.7: EM velocity model and an illustration of the ray-paths of upwards propagating waves. Velocities in m/ns

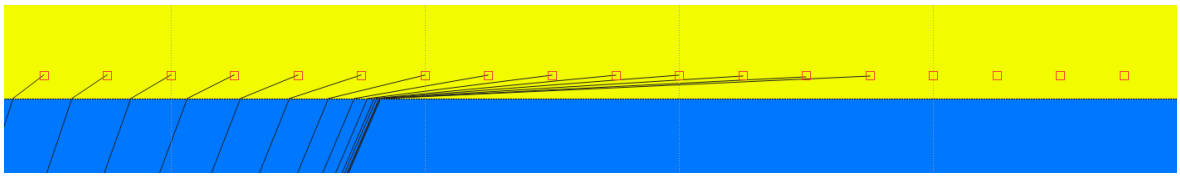

FIGURE 2.8: The air-solid boundary in figure 2.7. Some of the receivers do not detect the upwards propagating waves at all, because the critical angle restricts any ray from following a path reaching them.

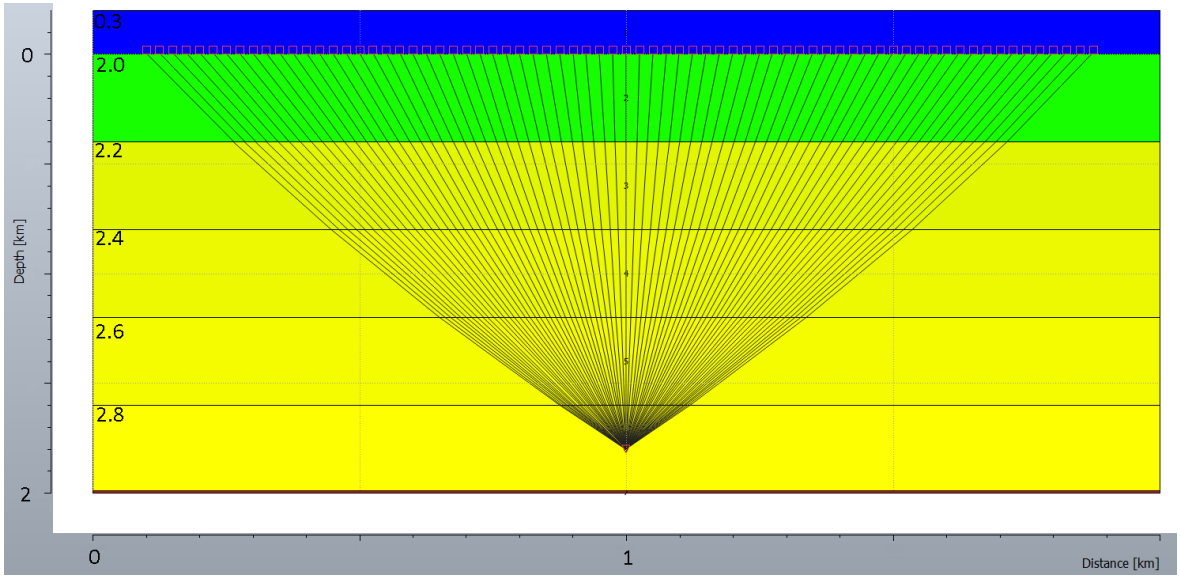

FIGURE 2.9: Seismic velocity model and an illustration of the ray-paths of upwards propagating waves. Velocities in km/s

2.2 Modelling based on outcrops

Creating models of a medium based on orthorectified exposed rock, and generating synthetic data based on them, is an established practice (Andersen, 2020). The principles of this project are the same as that practice, but with certain differences. Both in seismic and in GPR, the outcrop-to-model approach may suffer from the fact that the features present in the outcrop do not properly represent the media in 3D. As discussed in section **??**, the lateral resolution of GPR will tend to be worse than in seismic, and this should be accounted for when modelling.

A key difference from the seismic outcrop-to-model approach is that reflective boundaries do not necessarily give similar amplitude in GPR and seismic, and may infact not give any reflection at all, as the two do not directly rely on any of the same parameters. For this project large scale models were drawn based on a photogrammetry model of an outcrop by the Wordiekammen Plateau. And small scale models were drawn based on photos of renovated remains of the medieval Lyse Abbey outside Bergen. For both the large and small scale models, the real GPR-profiles for comparison have been gathered directly beyond the exposed rock (the large scale data was provided by NGU (Tveranger et al., 2020)).

Models were built with a simple approach. The photos of the outcrops were interpreted and divided into layers with assigned appropriate properties. For both the large scale and small scale models, all relevant dimensions were known. The only geophysical property used was the EM-velocity, directly dependent on the relative dielectric permittivity as given by formula 1.7. For the large scale Wordiekammen model, the average velocity had been estimated to be 0.11 m/ns by a CMP-analysis (Tveranger et al., 2020). For the small scale models, velocities were determined in a more arbitrary fashion, but in the ranges expected by rock and concrete one would expect based on table 1.2. In addition, analysing the GPR data collected at Lyse (in terms of approximate two-way-traveltimes through the media), velocities of around 0.09 m/ns seemed a reasonable approximation.

After building the models, the synthetic GPR images were generated by PSF-based convolution modelling. The method is exactly the same as in seismic data (Hagevold, 2019)(Andersen, 2020). The interference of waves from one reflector to others is present in all the real world GPR-data gathered and provided for this project. This interference naturally occurs as the interfaces are close and should be replicated in a synthetic dataset genrated by convolution modelling. However, in order for this effect to be reproduced, the model needs to be built with a high enough level of detail.

One step taken to achieve this was to automate a part of the interpretation, i.e. the color-codes of the photographed outcrops were used to assign the velocity properties of individual pixels, but only for portions of the models. Although this method returned a somewhat imprecise interpretation of the smaller scale brick-layers for instance, the resulting interpretation could be adjusted to reach a higher level of detail resembling the real photograph to an acceptable degree. In addition, this small scale auto-interpretation was only done to try and recreate the most chaotic parts of the signal. These small brick reflectors would not be expected to extend perfectly beyond the outcrop anyway. Also, it should be mentioned that the aim of this study was not to build high quality velocity models, but an attempt to test a modelling method.

2.3 Model Building

All velocity models, except the example model. Has been built by interpreting outcrop photographs (or outcrop models). All models were converted to their seismic velocity equivalents and dimensions according to table 2.1. These processes, along with the semi-automated simplistic interpretation described was performed with the MATLAB-script included in Appendix A. This script produces models in the SEGY-format, and the models are made with the seismic-equivalent properties. Because reflection coeffiecients of EM-waves are only directly reliant on dielectric impedance, the S-velocity of all models were set to zero. In addition, since density affects seismic reflectivity, density was set as a constant value through all models. A complete workflow of the modelling procedure, is shown in figure 2.10.

Populating the models with EM-wave velocities was done somewhat arbitrarily, but within the range of expected values from the dielectric constant of rocks as presented in 1.2. Additionaly velocities were mostly given as being close to the velocities determined as mean velocities for the two types of outcrop. 0.11 m/ns for the Wordiekammen outcrop, and 0.09 m/ns for the Lyse walls.

The Wordiekammen model was populated with two velocities only, 0.10 m/ns and 0.11 m/ns, both within the range of velocities of limestone. The smaller scale models were given velocities as follows: Concrete - 0.085-0.095 m/ns, soapstone/other rock - 0.10 m/ns, bricks - 0.09 m/ns.

2.3.1 Level of detail in the large scale model

:

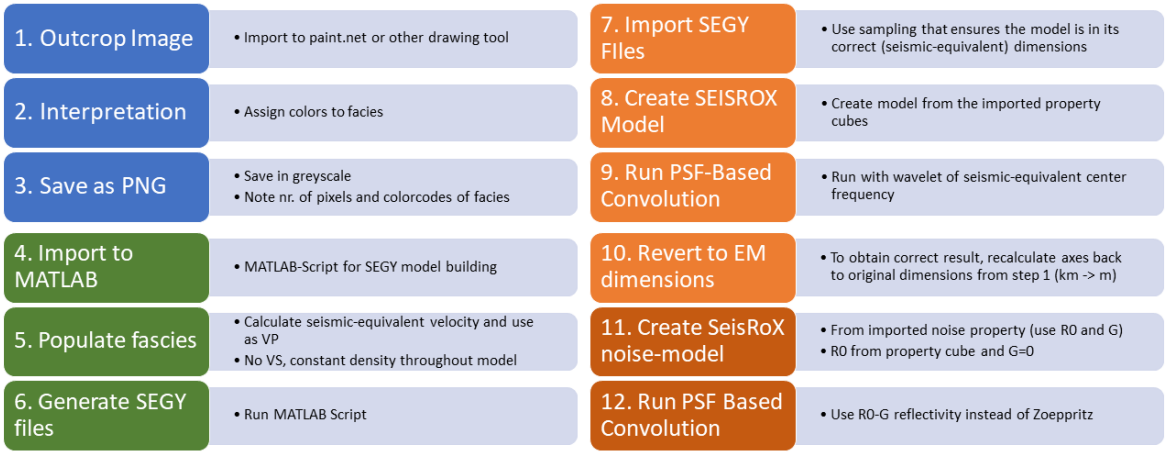

FIGURE 2.10: This figure shows the complete workflow of the modelling method. The first three steps were done using paint.net, the next three using MATLAB (copy of script included in Appendix A), and the final steps using NORSAR Software Suit and its SeisRoX modelling software. Noise models are only included for two of the outcrops in this study.

One of the challenges encountered when building models for the GPR-profiles. Are the level of detail needed in order to produce a realistic synthetic images from the model. For the 750MHz data, the outcrops are small scale, and with some effort they can be drawn as reasonable models. However for the 25-200MHz-data from Wordiekammen, the rock boundaries that are visible throughout the outcrop are separated by several meters. When drawn up as a model from the outcrop, the resulting model is not very detailed in some parts. Ideally, a high level of detail is wanted in order to properly test the PSF-based modelling method on this scale.

The outcrop does however show some smaller scale layers at certain locations. Figure 2.11 shows a line of height 10 m drawn on the Wordiekammen outcrop model. This is the separation between two boundaries available throughout the outcrop. The layer between these boundaries does however contain sublayers of a dimension of approximately 1 m and lower. In order to generate a better synthetic GPR image, these details should be included, but this level of detail is not available throughout the outcrop. For this reason specific section of the outcrop shown in 2.11, has been included in the interpretation, and the resulting models. This part of the outcrop was too deep to be captured by the real GPR survey.

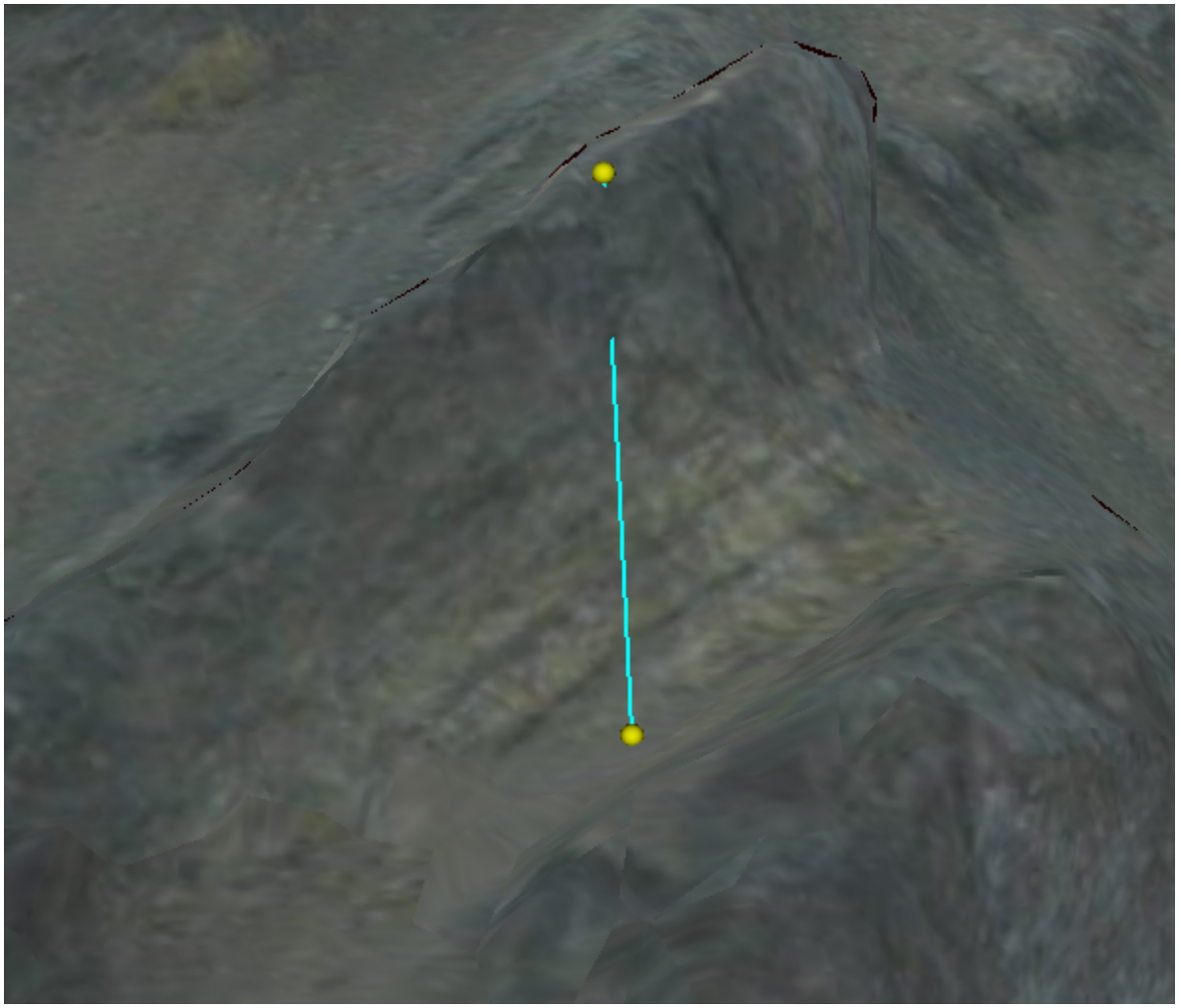

FIGURE 2.11: Illustration of the level of detail visible at certain parts of the Wordiekammen outcrop.

2.4 Real data collection

2.4.1 Wordiekammen

The large scale GPR profiles presented here were gathered on the Wordiekammen Plateau as part of a larger study on paleokarst structures, such as breccia pipes. The study was conducted for the Geological Survey of Norway and includes common-offset GPR profiles, CMP-analysis, and resistivity measures (Dalsegg, Elvebakk, and Rønning, 2005). For the purpose of outcrop-comparison, the data collected in this project is well suited, as it includes a photogrammetry model of the relevant outcrop and the plateau above (shown in

2.4.2 Lyse Abbey

At the Lyse Kloster site the restored ruin walls of approximately one meter height served as outcrops for models. The advantages of the walls for data collection was a clear vertical exposed stone that can easily be replicated as a model. Also, the walls made for very accesible data collection. The most obvious disadvantage of this site is that there is an uncertainty of how far the exposed rock extends perpendicularly to the profile (the y-direction, or beyond the outcrop). In order for the outcrop approach to be valid, it is desirable that the collected profile contains as few features as possible that are not visible on the outcrop, since that is the basis for building the model. The surveys were performed using a MALÅ GX750 georadar with a hip-chain as the shot-trigger.

A report on the condition of this site states that the resauration efforts performed in the 1920's and 1950's utilized various wall building techniques (Hagen, 2012). In some settings using original soapstone and other rocks, and in others using thinner slates to cover the side wall. The latter approach is not favorable for the purposes of this study, as parts of the visible wall face would not extend far in to the wall. However, the wall interior is more or less uncertain in any case, and the walls should not be viewed with the same reliability as a geologic outcrop.

One of the features contained in the outcrops are boundaries between the original rock and the smaller bricks from 20th century restoration. This feature does not extend through the wall for all cases but could still be expected to give some response detectable in the GPR-profile.

Assuming a mean velocity of 0.09 m/ns, the 750 MHz survey should give a vertical resolution of approximately 3cm and a lateral resolution of approximately 18cm at a 50cm depth (by equations 2.5 and 2.6. This means that features such as rock-cement,

FIGURE 2.12: The workshop wall.

rock-rock and air-solid boundaries should be expected to be visible in the profiles to some degree. Very detailed features, such as individual bricks, should not be expected to be detectable. They should however be expected to have some effect on the results. Increasing the detail included in the model will approximate the result closer to the the gathered data, but only up to some point, because of the earlier mentioned weaknesses of these outcrops. Processing of the gathered GPR profiles should improve the resolution somewhat.

The Workshop Wall

This wall contains some features that one might expect to show up in a GPR profile. Namely, the boundary at the bottom of the biggest rock, and the transition from original rocks of varying size to more uniform restoration bricks. The latter proved to be harder to detect than initially expected. Possibly because the boundary does not extend perfectly orthogonally through the profile. This could also be because the boundary is not a high permittivity contrast, and thus any reflection will have a low amplitude. The profile gathered on this wall was 3.77 m long, and the wall itself was a little under 1 m tall. It is shown in figure 2.12. The partial interpretation of this figure, with the smaller bricks left to be automatically interpreted, is shown in figure 2.14. A view of this wall from its side is shown in figure 2.13

The Kitchen Wall

This wall contained some large rocks, as well as a small brick portion. The extension of all features beyond the face of the wall was uncertain, as none were visible on the other side of the wall. The profile gathered on this wall was 2.59 m long, and the wall itself approximately 0.8 m tall. It is shown in figure 2.15. The partial interpretation of this figure, with the smaller bricks left to be automatically interpreted, is shown in figure 2.16.

FIGURE 2.13: The workshop wall viewed from its side.

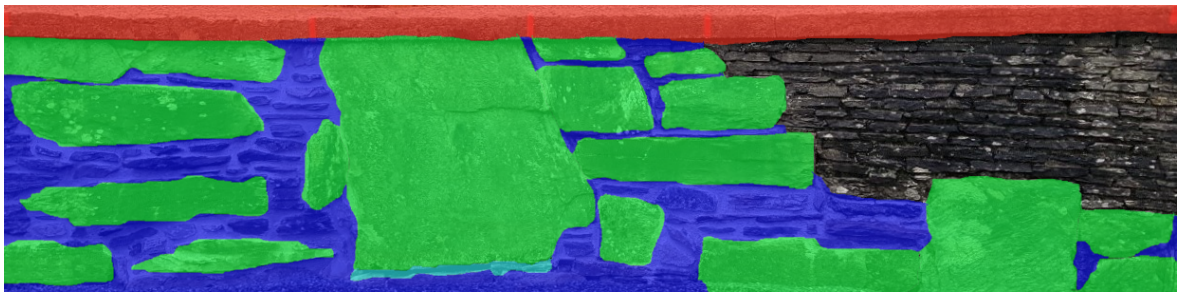

FIGURE 2.14: The partially complete interpretation of the workshop wall.

FIGURE 2.15: The kitchen wall.

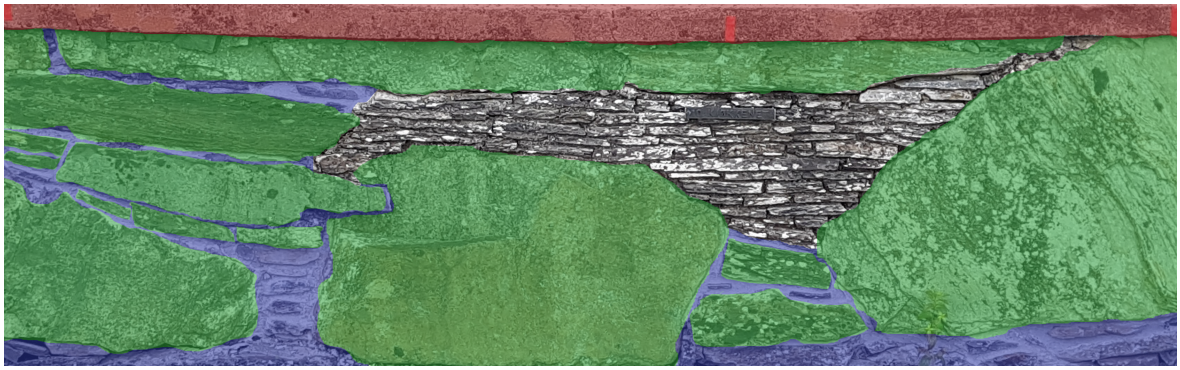

FIGURE 2.16: The partially complete interpretation of the workshop wall.

FIGURE 2.17: The Chapterhouse Wall

The Chapterhouse Wall

The brick layer on this wall extended throughout the wall, but any interface between it and the underlying rocks was hard to detect in the actual profile. The profile gathered on this wall was 2.37 m long, and the wall itself approximately 1.10 m tall. It is shown in figure 2.17. The partial interpretation of this figure, with the smaller bricks left to be automatically interpreted, is shown in figure 2.18.

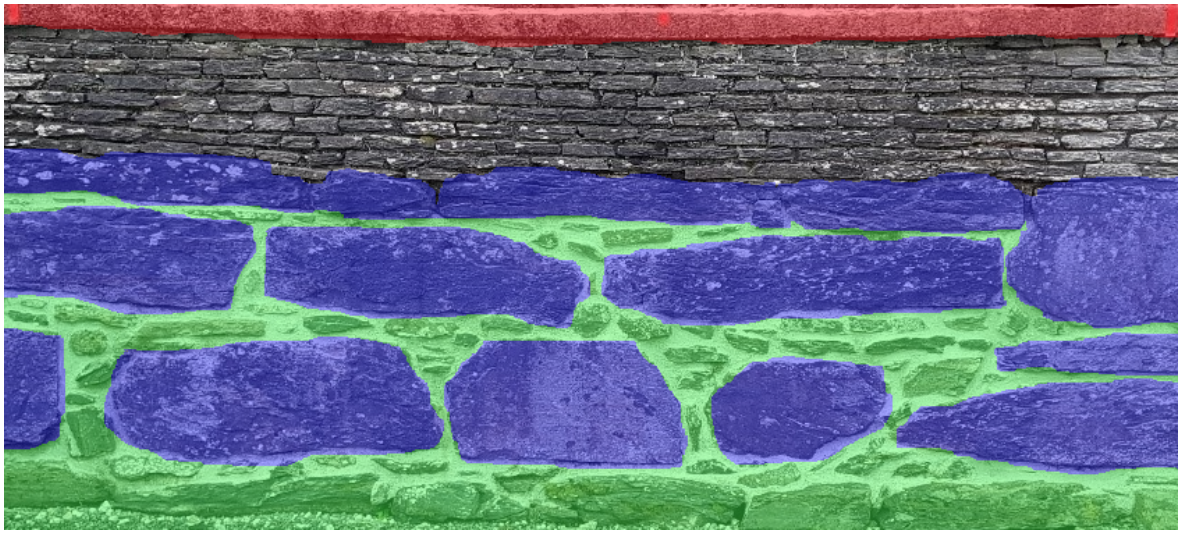

FIGURE 2.18: The partially complete interpretation of the chapterhouse wall.

2.5 Processing of datasets

The processing of the GPR-profiles included here were done on the principle of simplicity over complexity, but still with the aim of retrieving some resemblance to observable features from the datasets. The processing was done by the steps in figure 2.19.

Dewow is an important step in GPR processing, and is done to remove the direct-current (DC)-component, which is arises because of the proximity of the source and receiving antenna. It is in practice a mean-subtraction of the traces.

The start-time correction, as performed here, takes in information from the previous step, and automatically adjusts the 0-point of the traces by removing the initial part where little to no signal arrives.

Further a gain signal is applied to the traces, this was not done on the basis of any analysis of the actual attenuation affecting the data. But rather determined through trial and error to find a fitting gain function, strengthening late arrivals without having them overpower the early ones.

A Butterworth filter was applied to all traces, this was done in order to strengthen the signal-to noise-ratio. For the 50 MHz data this was done with a frequency window 25-75 MHz. For the 25 MHz data a 10-40 MHz window was used. For the smaller scale data, the window varied somewhat from profile to profile, but was around 400-1100 MHz.

FIGURE 2.19: The partially complete interpretation of the chapterhouse wall.

For most of the profiles, the penultimate processing step was the Stolt migration. The purpose of this processing step is to correct features such as hyperbolas, caused by point reflectors. Migration can also be used as a tool to estimate the velocity of a medium, by finding which velocity best collapses hyperbolas in to points.

Topographic correction, a three step process including topographic migration, was only done for two of the profiles presented here (in figure 3.21). These results were not well suited for comparison to the modelled data (which was built with the outcrop slightly on a slant), but have been included anyway, to display that the profile did in fact have some elevation (approximately 15%). For this reason it has been greyed out in the workflow. Last, a time-depth conversion was done, correcting the axes of the figure to correctly display depth instead of time.

Chapter 3

Results

All modelling results generated by the PSF-based method, as well as real GPR profiles, are presented below. The results are mainly sorted by the effect they demonstrate: Frequency variation, bandwidth variation, illumination variation and pulse variation. For some of the synthetic data, the PSF is included, and shown in its correct scale in relation to the synthetic image (0.4 x 0.4 m for the small scale data and 20 x 20 m for the large scale data). In figures 3.5 and figure 3.12, the PSFs have not been shrunk down to fit the image dimensions, this in order to highlight small differences that were more visible in the PSFs themselves than the images.

3.1 Varying Center Frequency

Increasing the central frequency of the source pulse will lead to a better resolution, as smaller and smaller details can be detected. This is true in both seismic and GPR surveys. And just like in seismic, one can calculate the theoretical resolution both vertically and horizontally, as is shown in equations 2.5 and 2.6.

From these formulas, only the horizontal resolution is dependent on depth (not accounting for the fact that attenuation will affect high-frequency signals more than low-frequency ones, and in turn worsen the vertical resolution as well). This is shown in figure 3.1. The effect of velocity, although small, will be captured in the modelling results. However, this effect of a better resolution for lower velocities will be outweighed by the severe restriction on the illumination pattern caused by low velocities. This effect is discussed in section 2.1.2 and demonstrated in section 3.3.

To display the effect of varying the center frequency, the velocity model of the chapterhouse wall was used. Convolution modelling was performed on this model using gaussian pulses with 500 MHz, 750 MHz and 1000 MHz center frequency. The outcrop is shown in figure **??**, the model in figure 3.2, the modelling results in figure 3.3, and the real GPR profile in figure 3.4.

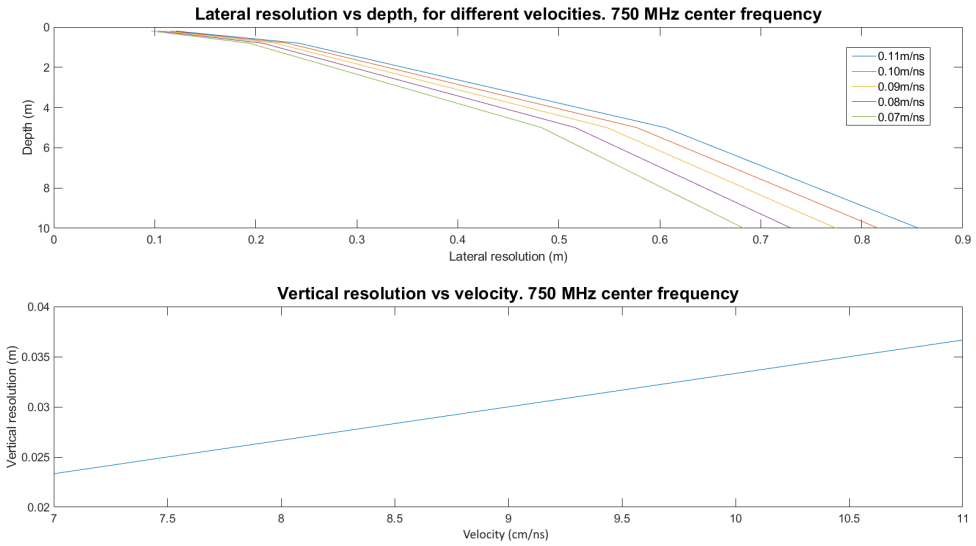

FIGURE 3.1: Lateral and vertical resolutions as functions of depth (and velocity).

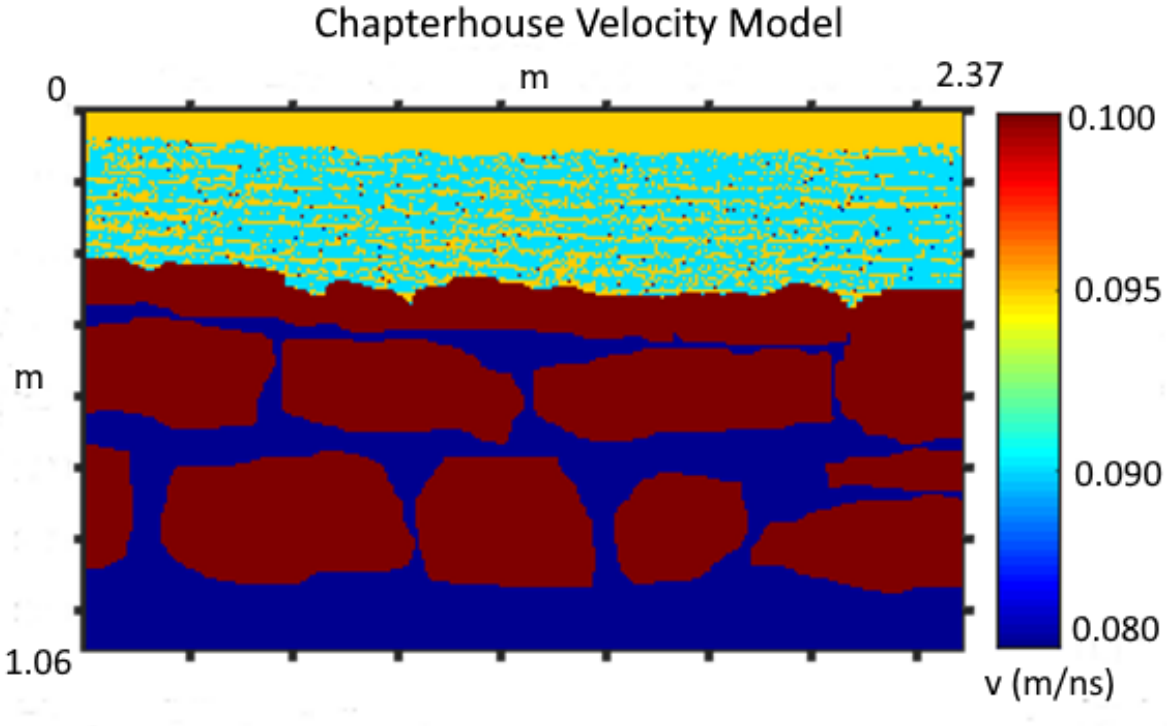

FIGURE 3.2: The velocity model of the chapterhouse wall. In its seismic equivalent values. Velocities as VP, VS=0 and density constant

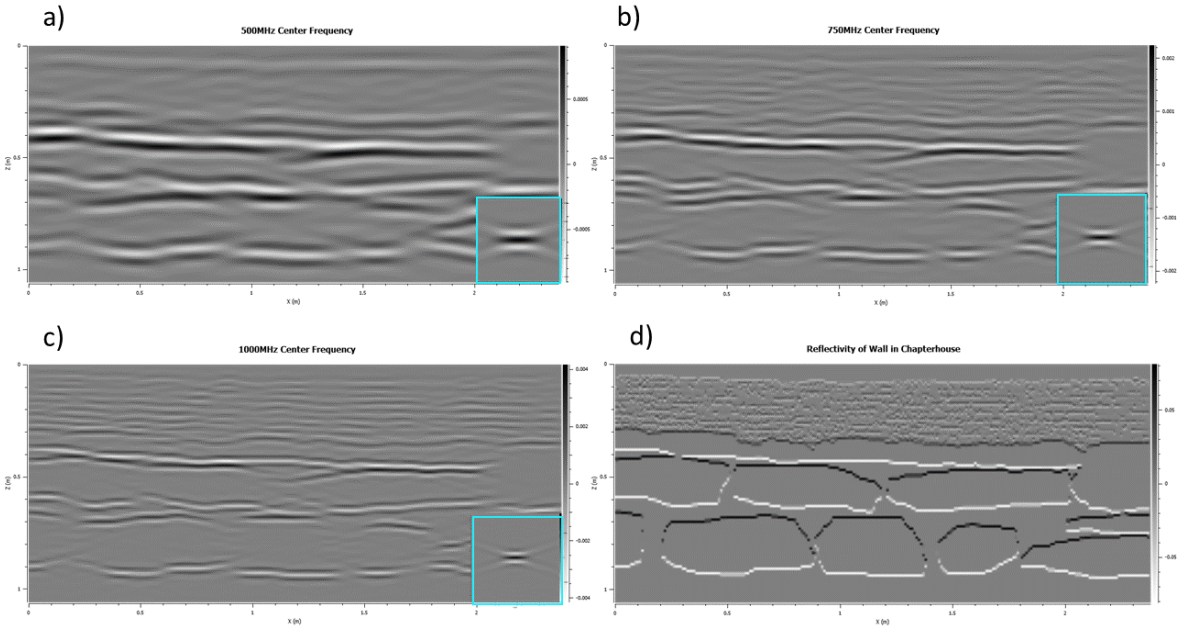

FIGURE 3.3: Convolution with 500 MHz, 750 MHz, 1000 MHz. The corresponding PSFs are to scale.

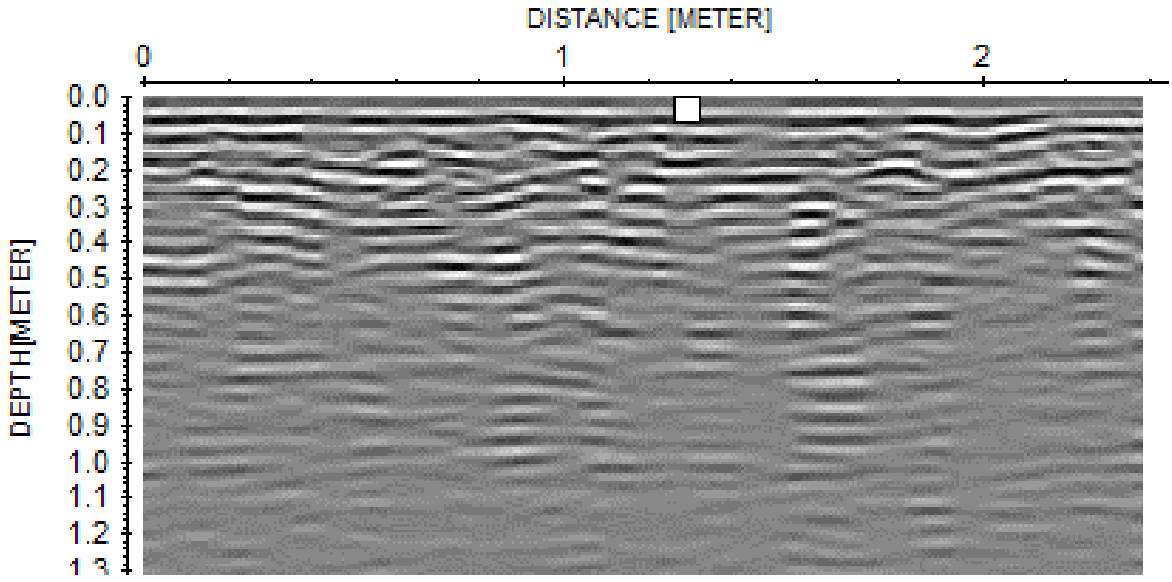

FIGURE 3.4: The real data GPR profile of the Chapterhouse Wall.

3.2 Varying Bandwidth

As the bandwidth of a pulse increases, the pulse becomes shorter in time. This should cause the convolution result to become sharper. To display the effects of varying the bandwidth, the chapterhouse model was used again, as well as gaussian pulses with approximately 100 % and 150 % fractional bandwidth (at 10dB loss). The effects of the increase in bandwidth are not very pronounced, but can be seen more clearly in the PSF images (figures 3.5 b) and d)).

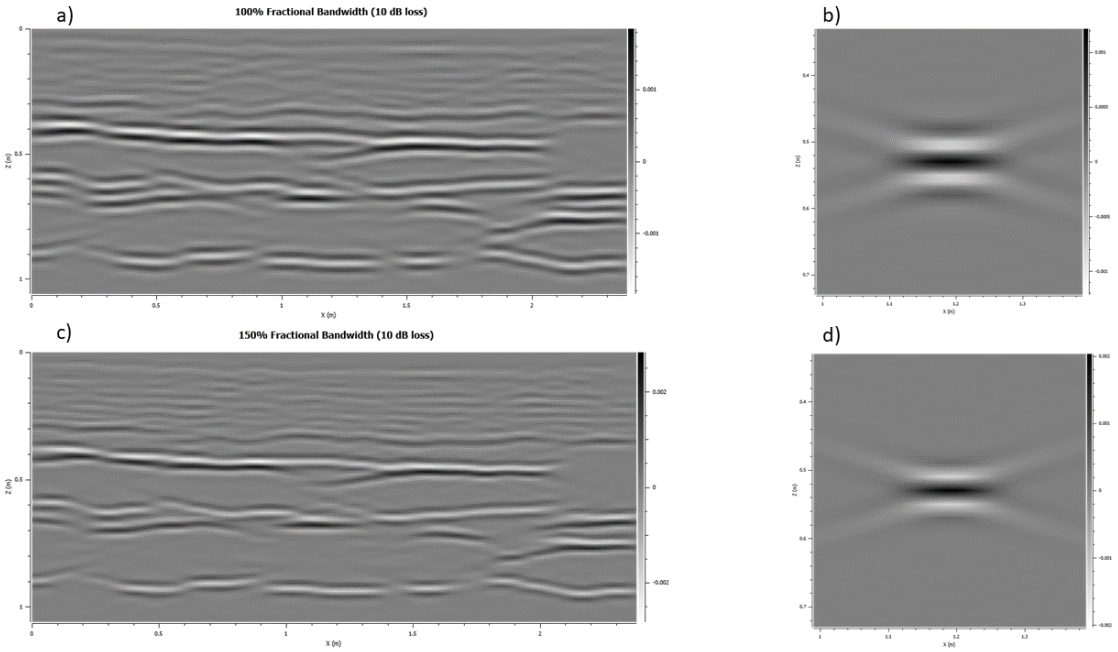

FIGURE 3.5: Modelling results for 100% and 150% fractional bandwidth and their corresponding PSFs (not to scale).

3.3 Varying Degrees of Illumination

As discussed in 2.1.2, an important difference between seismic and GPR is the narrow illumination pattern caused by the velocity contrast from air to rock or soil. A simple example of a velocity model and rays reaching the surface is shown in figure 2.7. Figure 3.6 shows how the decreasing velocity will seriously reduce the maximum take off angle of waves in this model. The maximum take off angle in this context is the widest angle with which waves can travel towards the surface and be detected there (with 0 deg being the vertical path.)

Since no waves transmitted over the maximum take off angle will be detected at the surface, no reflector with an angle greater than this angle, relative to the surface, can be detected. Three angles from figure 3.6 have been chosen to visualize the narrowing illumination effect. 21.5 °, 17.5 °and 13.5 °. Corresponding approximately to 0.11 m/ns, 0.09 m/ns and 0.07 m/ns, respectively. The velocity model of the kitchen wall will be used, shown in figure 3.7. A 750 MHz centre frequency gaussian pulse with 120 % fractional bandwidth will be used for all angles.

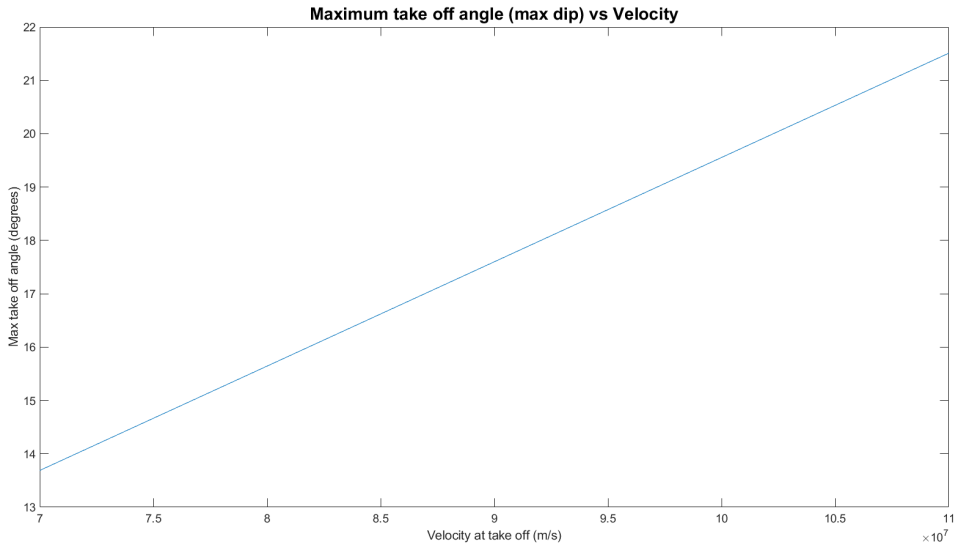

FIGURE 3.6: The figure shows the maximum take of angle of a ray following Snells law through a velocity model like the one in 2.7. These values have been calculated from an initial critical angle of 21.51 deg as the wave is transmitted from air (0.3 m/ns) to a rock with velocity 0.11 m/ns.

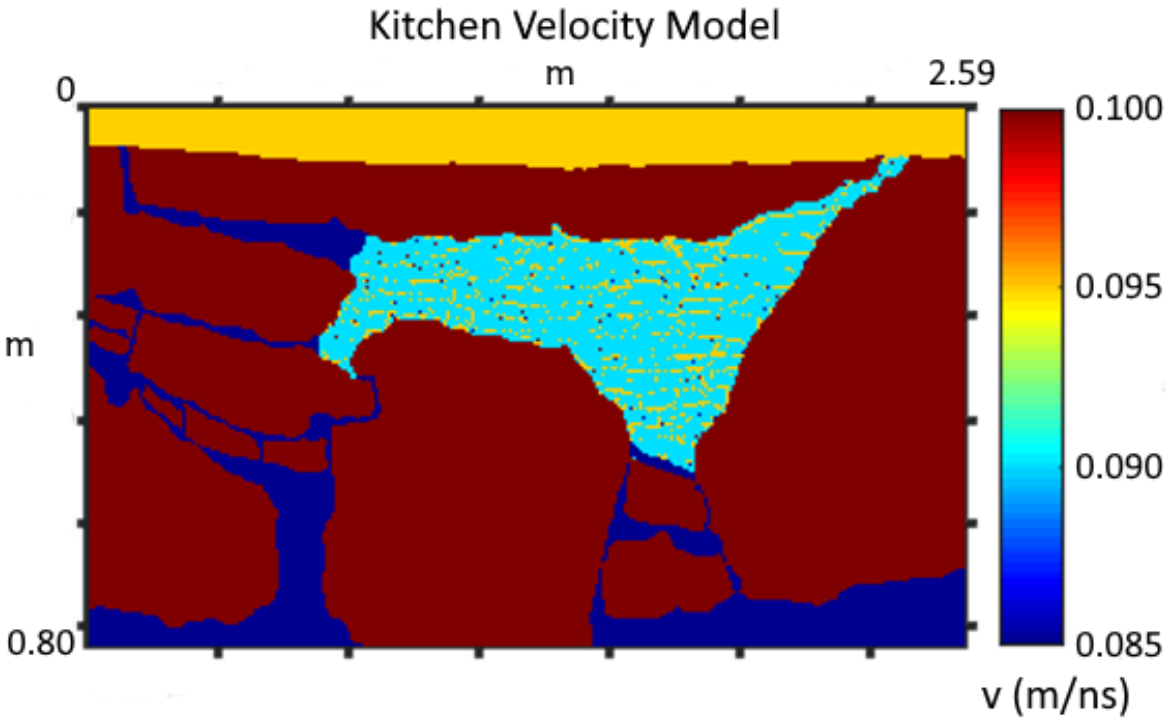

FIGURE 3.7: The velocity model of the kitchen wall.

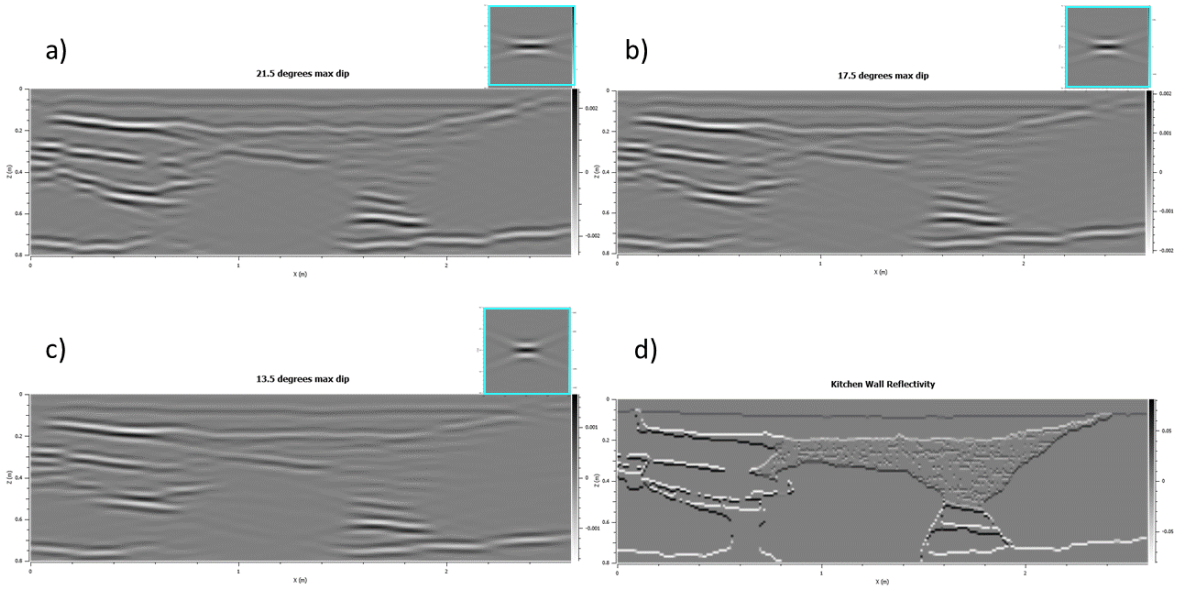

FIGURE 3.8: Convolution results for different angles of illumination. The PSFs are highlighted in light blue, they have dimensions 0.4 x 0.4 m, and are shown in scale relative to the images.

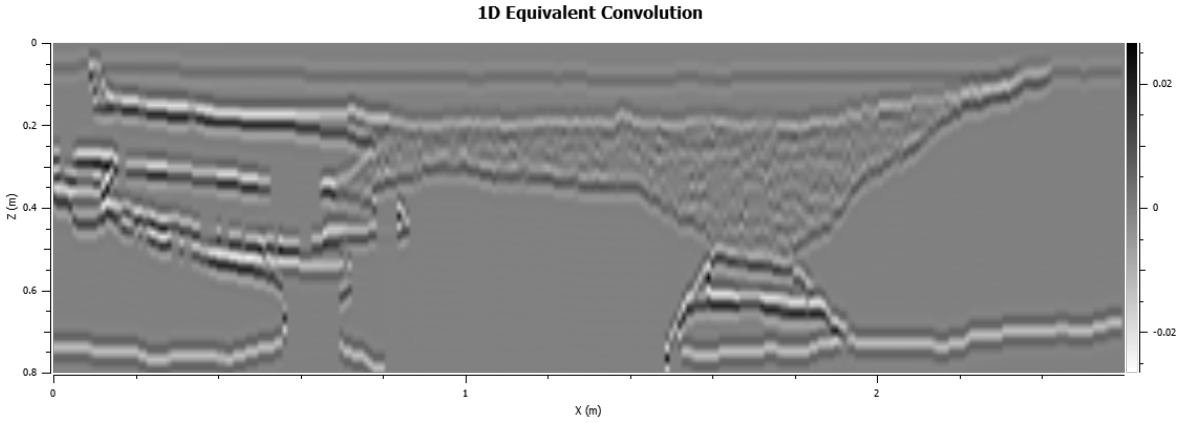

FIGURE 3.9: Repeated 1D-convolution to create an image in 2D. The lateral resolution is overestimated.

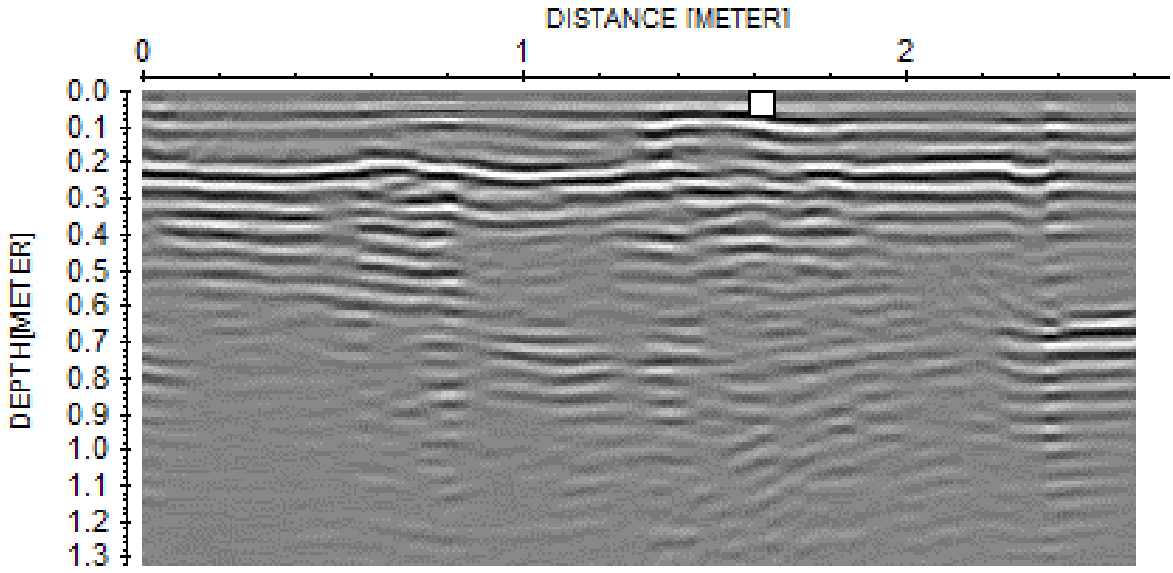

FIGURE 3.10: The real data GPR profile of the Kitchen Wall.

3.4 Comparison of Extracted and Synthetic Pulse

The shape of the pulse used in the convolution will have an effect on the result. From the real GPR data collected over the workshop wall. A part of a trace which was interpreted to possibly resemble source pulse was extracted. This pulse was resampled, to be smoother, and normalized, in order to be more comparable to the synthetic gaussian pulses used in this study. This pulse and its frequency content is shown in figure 2.5. To display the effects of using the extracted pulse, versus the synthetic gaussian pulse, the workshop wall velocity model was used (figure 3.11. This model differs from the previously shown velocity models, in that it contains an air layer, which gives a much stronger reflectivity than the surroinding rock-to-rock interfaces.

The difference in the results produced from the synthetic and extracted pulse are marginal, but definitely visible when comparing their PSFs.

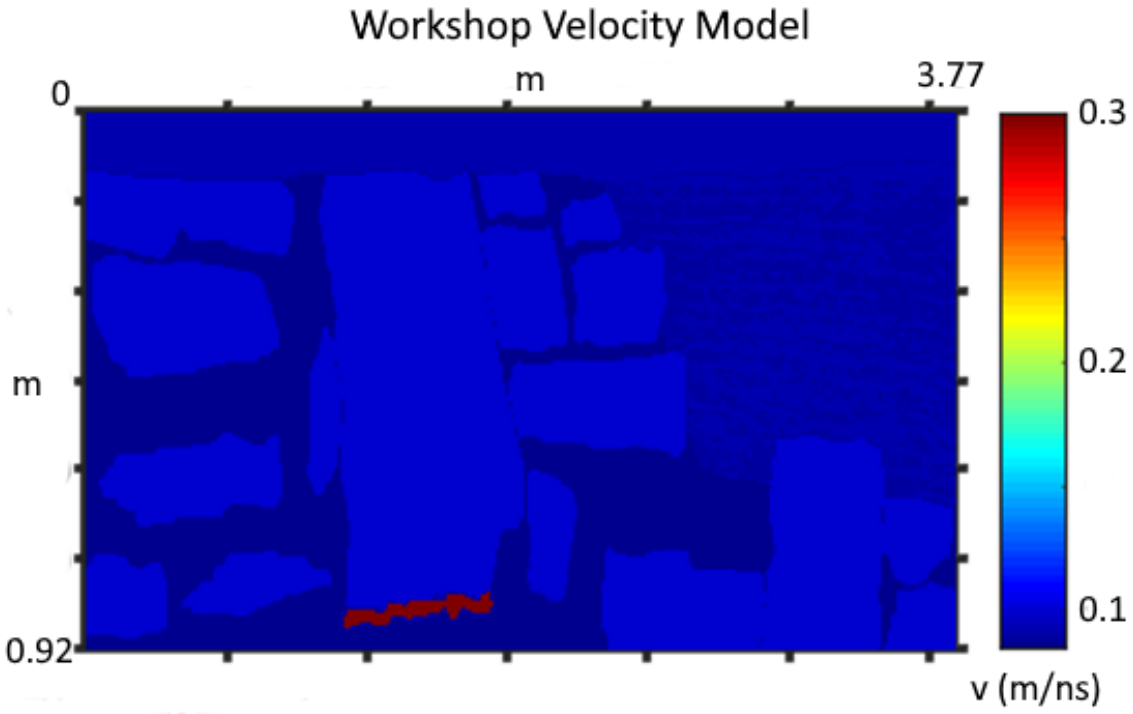

FIGURE 3.11: The velocity model of the workshop wall.

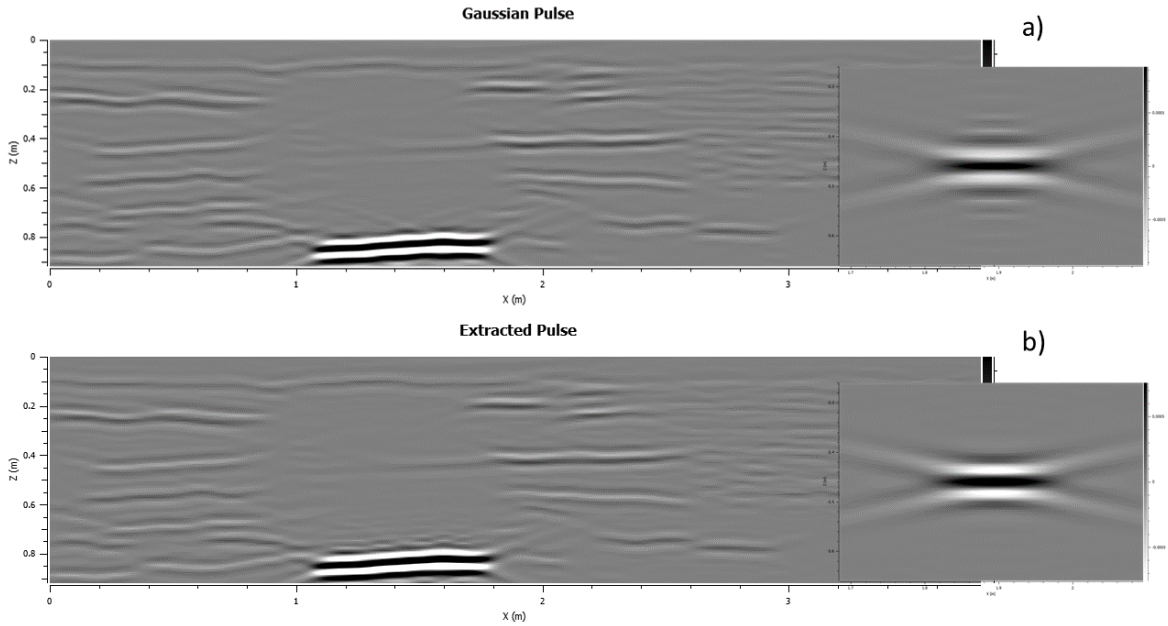

FIGURE 3.12: Modelling results for the synthetic and real pulses. PSFs not to scale.

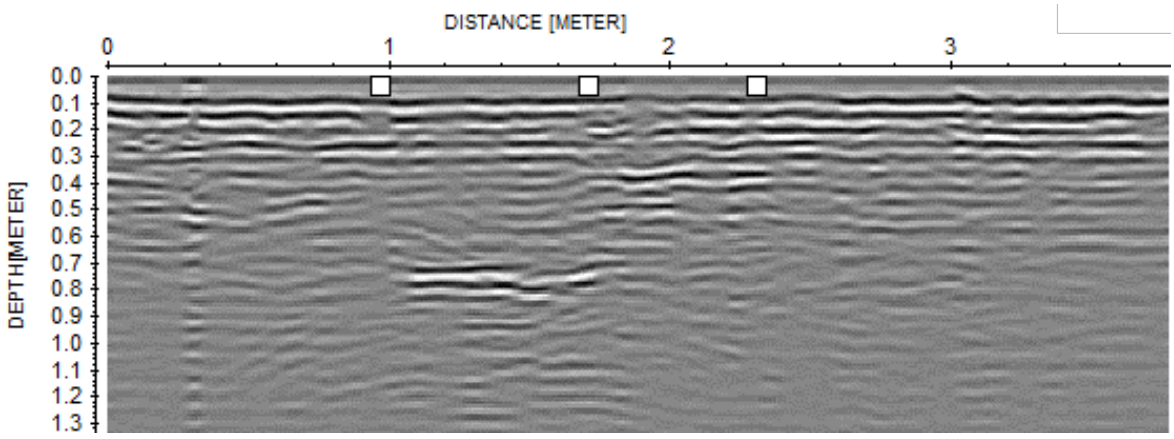

FIGURE 3.13: The real data GPR profile of the Workshop Wall.

3.5 Convolution with noise

In order to produce results more similar to actual GPR surveys, one can include noise. In this study, that has been done by convolving a source pulse over a reflectivity series consisting of white noise (initially reduced in reflectivity to 5%). The result of this process is shown in 3.14. Sections of pulses convolved over noise, with correct scales, can then be added to the synthetic convolution results. An example of this is shown in figures 3.19 and 3.15

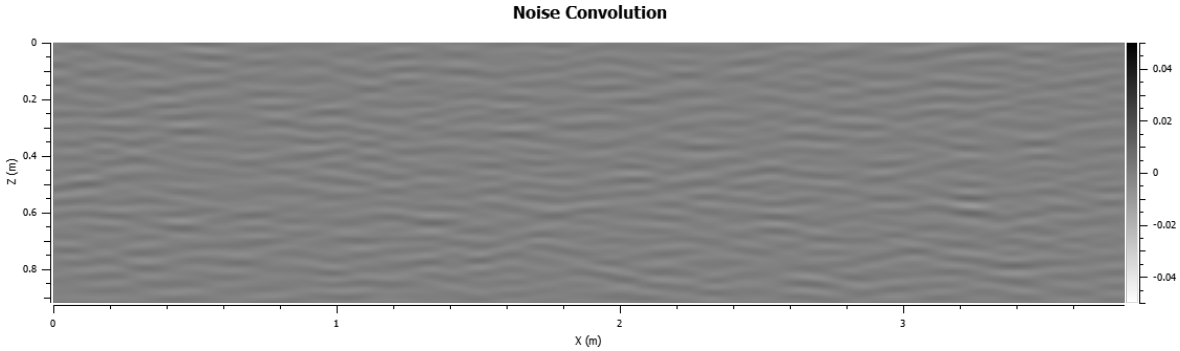

FIGURE 3.14: The result of a PSF-based convolution over a reflectivity model made up of white noise, with the same geometry as the workshop model results

3.6 Comparison of Synthetic data to Outcrop

Of all the profiles gathered at the Lyse site, the workshop wall was the one that showed the most resemblance from outcrop to GPR. One of the reasons being the air gap. Of the few features recognizable in the profiles, it was the one that stood out the most. This feature is much more dominant in the modelling results, because the method ensures that the relative amplitude of reflections is not affected by attenuation. Reproducing this for the real profiles would require some more detailed processing. For the purpose of this comparison however, the processing described in 2.5 should be adequate.

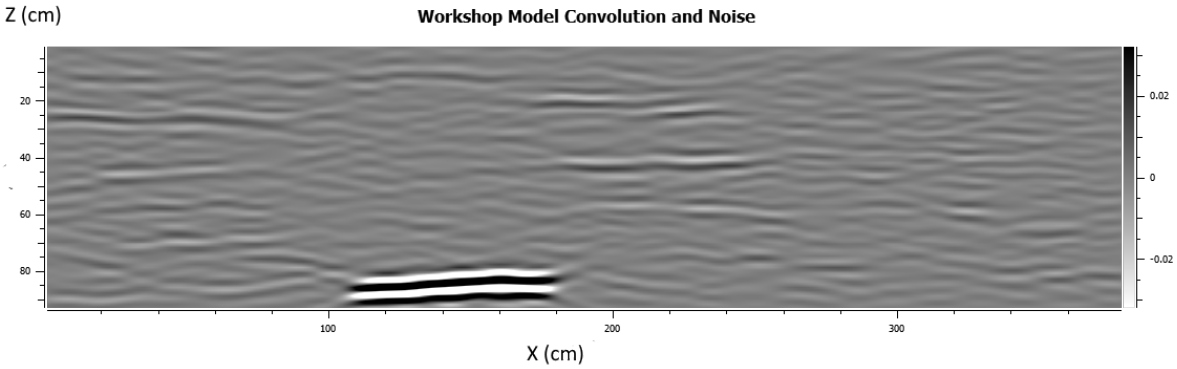

FIGURE 3.15: Final result of the workshop model, with noise. By 750 MHz center frequency, 120 % fractional bandwidth, and 17.5 °maximum dip angle.

3.7 Large scale GPR and modelling results

The Wordiekammen outcrop models were drawn with a greater depth than the penetration depth of the 25 MHz survey. This was done in order to include visible features on the outcrop below the penetration depth of the survey which were of interest interesting to model. A section containing a more detailed interpretation, and reflectivity, and the modelling results that arose from this section, is discussed in section 4.1.2.

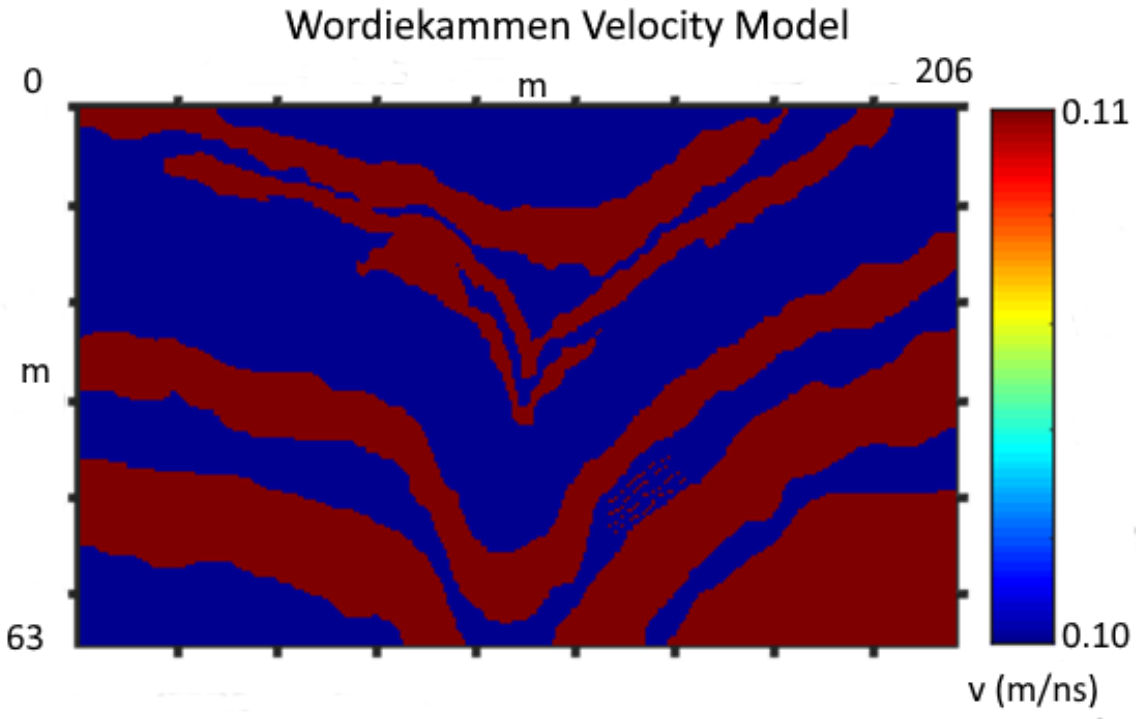

FIGURE 3.16: The Wordiekammen velocity model.

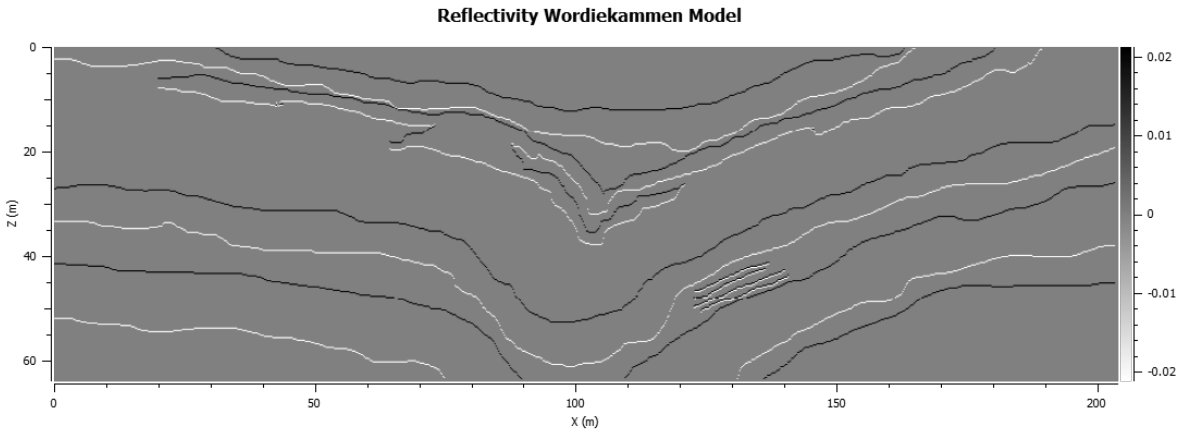

FIGURE 3.17: The Reflectivity Model resulting from the velocity model in figure 3.16

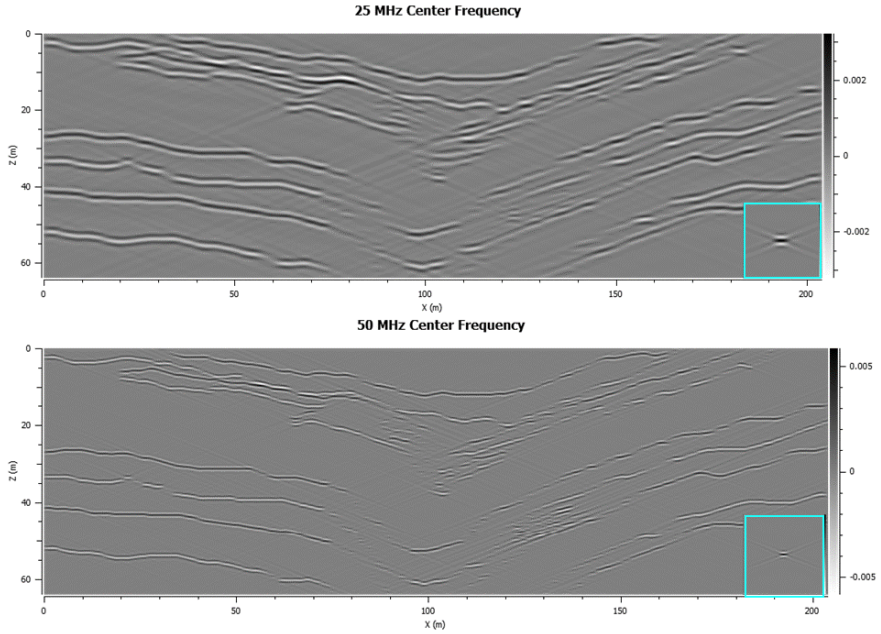

FIGURE 3.18: Results of the PSF convolution of the Reflectivity Model in figure 3.17

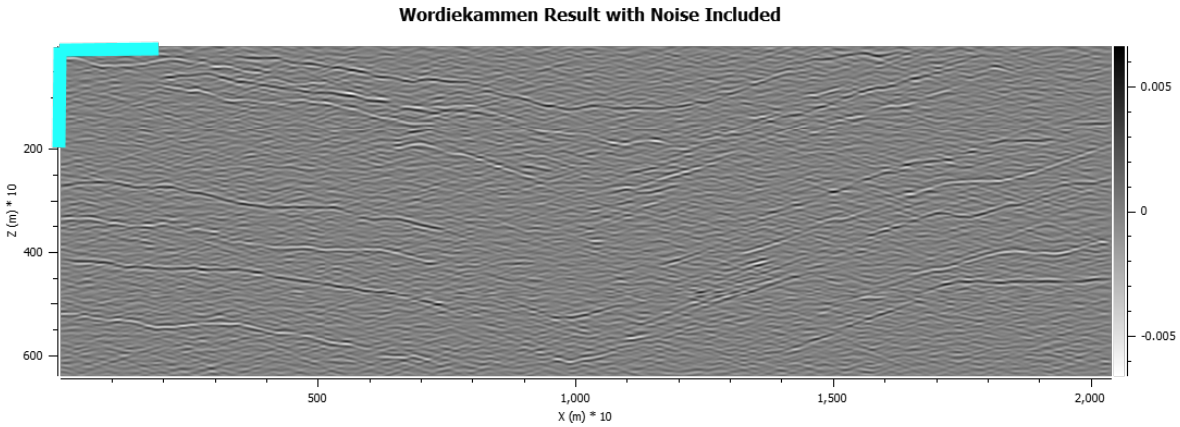

FIGURE 3.19: The result from figure 3.18, with noise. The blue lines are in the same scale as the PSFs, and serve as a scale for this figure (20x20 m).

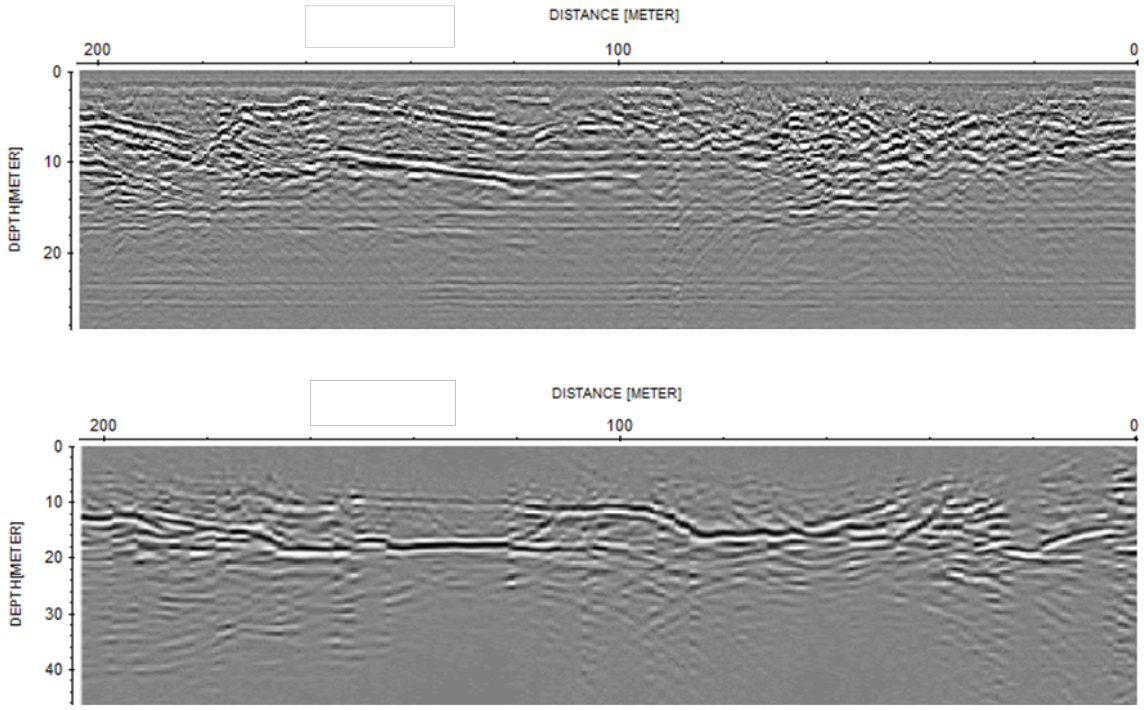

FIGURE 3.20: The GPR profiles gathered at the Wordiekammen Plateau, with 25 MHz and 50 MHz. These profiles have not been topographically corrected, as they are somewhat easier to compare to the modelled results. The topographically corrected profiles are shown in 3.21

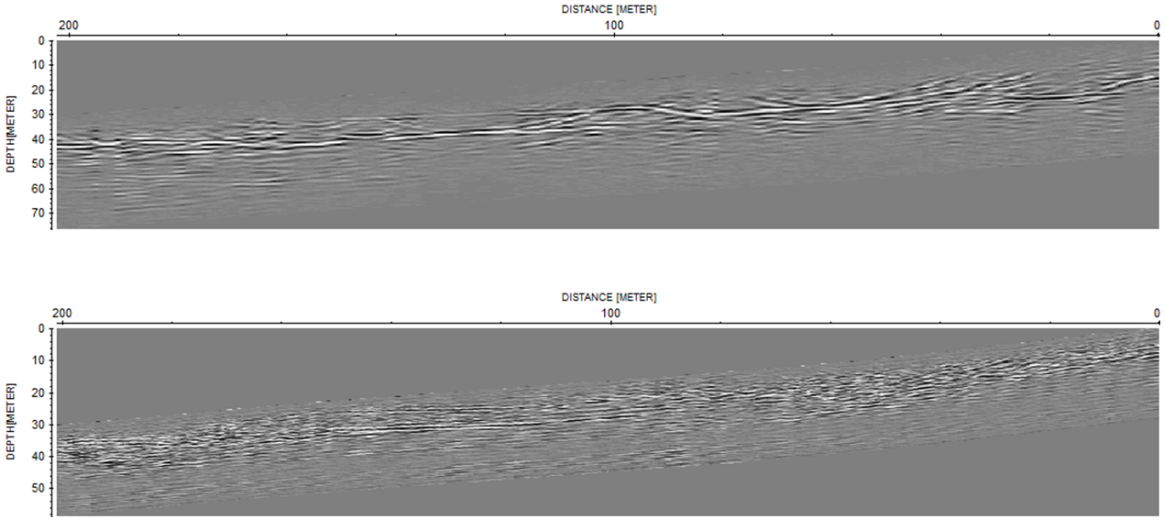

FIGURE 3.21: The topographically corrected GPR profiles gathered at the Wordiekammen Plateau, with 25 MHz and 50 MHz

Chapter 4

Discussion

4.1 Assessing the results

4.1.1 Assessing the results

The results presented in this study shows the application of the PSF convolution modelling method for different scales, as well as real, processed, GPR profiles in corresponding scales. Varying frequency, bandwidth, illumination, and velocity contrasts are explored in the modelling results. All velocity models used in the study, except for the example in figure 2.1, are presented.

The effects of some processing steps are shown, although to accurately process the data to resemble the modelling results is very difficult. There are several reasons for this. Most important is perhaps the fact that the real GPR profile is a result of a real medium, while the synthetic data is based on a 2D velocity model that may or may not be valid. In addition, as already discussed earlier, the modelling method produces results as if they were not affected by attenuation. Real GPR data on the other hand are always affected by this, and must be processed accordingly.

The weakness of repeating 1D-convolution is also shown, in figure 3.9. This figure illustrates how the result of the simplistic approach resembles the reflectivity series much more than the 2D results. The reason for this is that the 1D-convolution overestimates lateral resolution (Eide et al., 2018). Comparing the 1D result to the real GPR profiles shown in this study shows that it is not a well suited approach here, especially because of the lateral resolution limitations on GPR data.

The modelling method was very effective in terms of calculation times. For example, the large scale wordiekammen images were generated in approximately 7 seconds per image (4096 x 2048 samples).

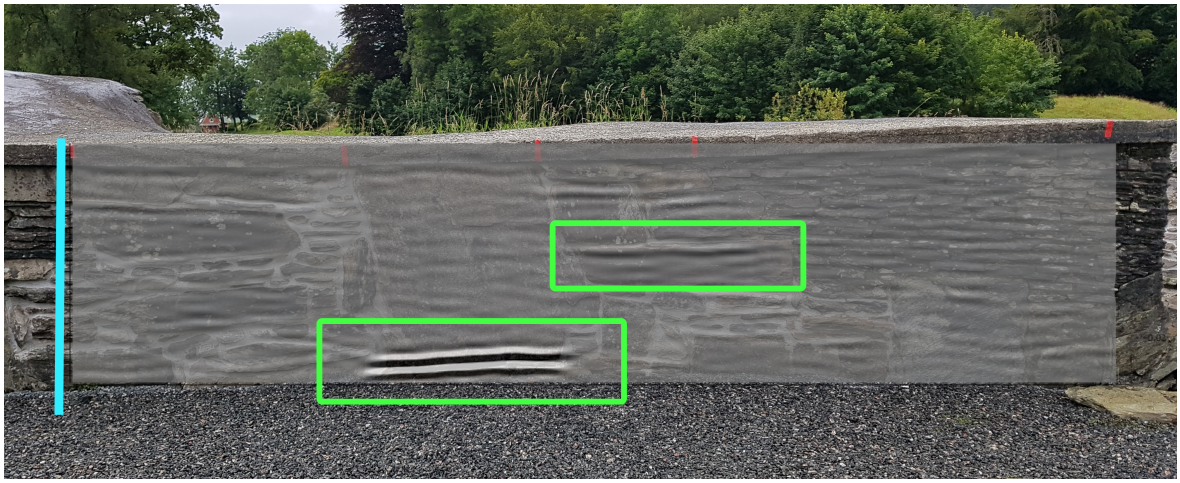

FIGURE 4.1: This figure shows the synthetic GPR image generated for the workshop wall model, superimposed on the wall itself. The light blue line is 1 m long, and the profile is 3.77 m long. The reflectors highlighted in green are known to come from an air-rock boundary and an air-concrete boundary, because they are a result of the reflectivity model.

4.1.2 Interpreting the results

All the synthetic datasets shown in this study bear at least some resemblance to their respective outcrops, because the velocity models were created solely on the basis of those outcrops. For the real data, the profile that had the most resemblance to its outcrop was the profile gathered on the workshop wall, an interpretation of this profile, superimposed on the actual outcrop, is shown in figure 4.2. This interpretation is not necessarily correct, but the reflection interpreted as the air gap was so strong that it was visible in the raw data. The other reflection, which is interpreted as being from a rock-rock or rock-concrete interface, but may infact be a reflection from something not visible on the face of the wall, such as another air gap in its interior. The bottom of the top concrete-layer seal may also be visible in several of the small scale profiles as an early reflector. But this interpretation is more uncertain, because of its proximity to the surface, where processing may have shifted it somewhat from its expected time of arrival. In addition vertical resolution makes it difficult to determine certainly where this reflector occurs. All the small scale real data is dominated by horizontal reflectors, which may be caused by the restricted ability to detect dipping reflectors.

For the large scale data from the Wordiekammen plateau, the profile was more difficult to interpret, in terms of connecting features in the outcrop to features in the

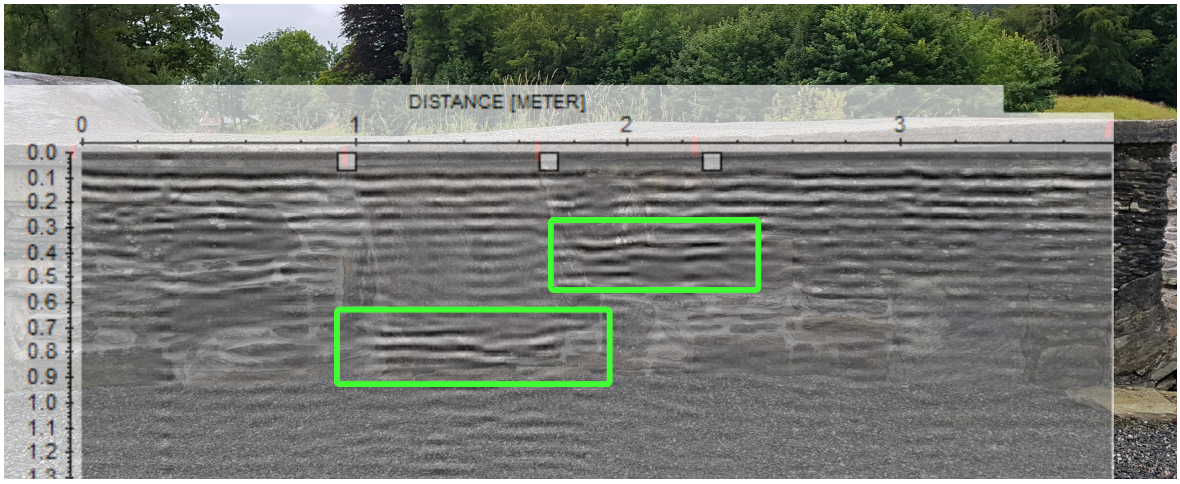

FIGURE 4.2: The real GPR profile gathered on the workshop wall, superimposed on the wall. The depth is in meters. The reflectors highlighted in green are interpreted as being the same as those highlighted in 4.1

data. There are breaks in the horizontal reflectors, which contain a more chaotic response. This is difficult to tie to specific features in the outcrop, and could be from collapse structures beyond it. The V-structure is hard to detect in the GPR-profile, possibly because of a low lateral resolution and its dipping reflectors.

The model for this outcrop (figure 3.16) includes a section of higher detail than the rest of it, with reflectivity representing the interbedding shown in figure 2.11. These layers, which are only visible in parts of the outcrop, are not visible in the real data, because of their depth. It is however of interest to see how this level of detail is modelled by the PSF-based convolution, for 25 and 50 MHz wavelets. This portion of the modelling results is shown in figure 4.3, and demonstrates the effect of small scale reflectivity. The wavelengths of the 25 MHz and 50 MHz signal in media of 0.11 m/ns are 4.4m and 2.2m, respectively. Using the assumption that the vertical resolution is a quarter of the wavelength (Annan, 2009), these layers fall below the range of resoltion for the 25 MHz convolution, however they still have an effect the data. The layers also slightly fall below the range of resolution of the 50 MHz convolution, mostly because of the way they have been drawn up for the model, as some are in fact definitely thicker than they have been drawn. Still they have a noticeable effect on the data, even though they can not be accurately separated.

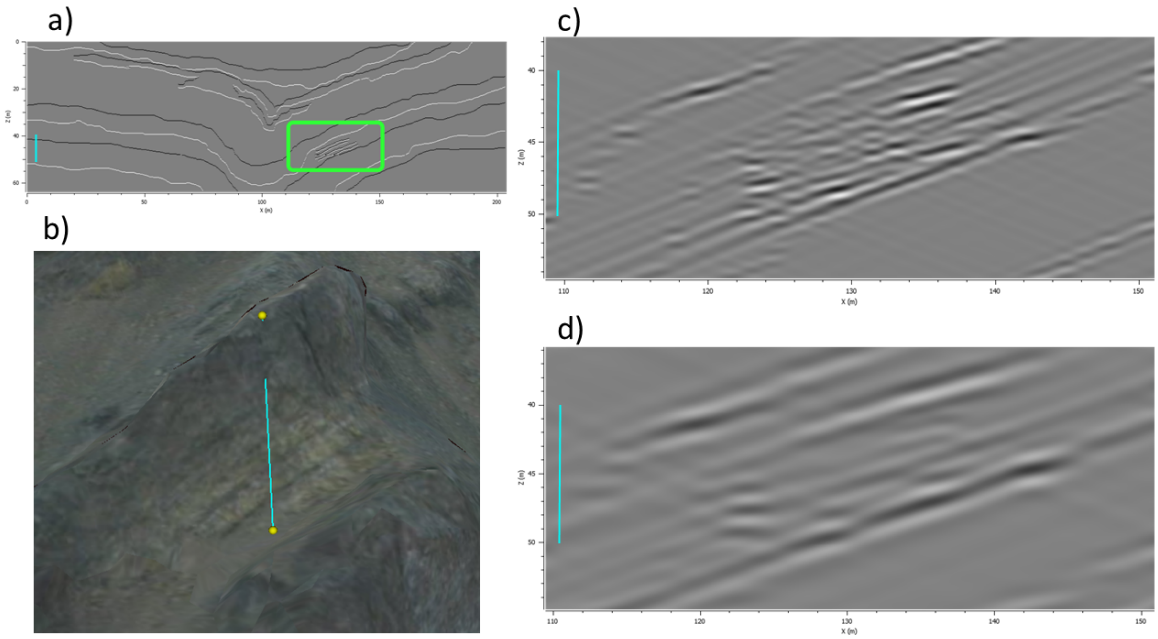

FIGURE 4.3: a) The reflectivity of the wordiekammen model, with the detailed interpretation highlighted in green. The light blue lines in all these figures are 10m long. b) The small scale layers, as shown in the outcrop. These layers are not visible throughout the outcrop. c) The 50MHz modelling result of the highlighted section (zoom from figure 3.18, which also shows the corresponding PSF). d) The 25MHz modelling result of the highlighted section (zoom from figure 3.18, which also shows the corresponding PSF).

4.1.3 Validity of outcrops for model building

One of the issues with interpreting the real GPR profiles and comparing them to the synthetic data is that the outcrops shown in this study might not be very reliable indicators of the 3D structures beyond, especially the small scale models, as demonstrated by figure 2.13. Some of these models should be expected to be more valid than others however, for example the chapterhouse model 2.18, where the brick layer appears to extend through the entire wall. The large scale wordiekammen model, on the other hand, is based on geological features, not man made walls with an uncertain interior. A study conducted near the outcrop presented here built 3D-models extending far beyond the visible outcropping, on the basis that the same features were detected by GPR as were interpreted from virtual outcrop models (Janocha et al., 2020). This does not guarantee that the outcrop presented here has the same traits, but it is an indication that one might expect something similar. In addition the survey report of the Wordiekammen data presented here states that collapse structures visible in the outcrop was possibly detectable further back than the included profile (Dalsegg, Elvebakk, and Rønning, 2005).

It should be mentioned that the models presented in this study is first and foremost intended to be a tool for testing PSF-based convolution of GPR data, not as a precise recreation of geologic features. This is true not only of the simplistic stratigraphic interpretation, but also of the velocities used to populate the models.

4.1.4 Validity of velocities and other geophysical properties

The basis for the wordiekammen velocities is described in section 2.3. The range of these velocities are justified by the CMP-analysis, and by known velocity values for limestone. The way the velocities are determined to fit the model on the other hand, is arbitrary. That is a definite weakness of the model, as well as using only two different velocities. The real GPR profile clearly shows that some reflectors are stronger than others, an effect that is not achieved by this two-velocity model.

For the Lyse models. There were no CMP survey to provide information about the velocity. An assumption made early in the analysis of the wall profiles, was that the mean velocity was in the 0.09 - 0-10 m/ns range. This assumption was made on the basis of the apparent two way travel time to the air gap in the workshop wall profile. Also, there was no indication from the profiles that there were any of the main materials present that caused large velocity contrasts, and in turn strong reflectivity, except air.

The attenuation effects of conductivity have not been directly modelled. Equation 4.1 shows how EM-waves are attenuated for non-dispersive frequencies (Annan, 2009), as a function of dielectric permittivity and conducivity. Modelling with different frequencies, such as in figure 3.3, is a limited way to display attenuation effects. This is because higher frequency EM-waves are attenuated faster than lower frequency ones, an effect also observed in acoustic waves. The modelling results for lower frequency sources can therefore be used to study the effects of attenuation for a given medium, with a given attenuation factor for some depth. Further studies testing the PSF-based convolution method for modelling GPR images with attenuation is suggested.

$$\alpha = \frac{1}{2}\frac{Z_0\sigma}{\sqrt{\kappa}} \tag{4.1}$$

4.1.5 3D effects

Although the real GPR profiles presented in this study are 2D-profiles, they are a result of incoming waves from three dimensions. This is a natural weakness of two-dimensional surveys, both in the GPR and seismic domains. In order to properly image complex subsurfaces, three dimensional surveys and processing is required. This does not mean that the smaller scales 2D profiles presented here are completely invalid, but it is very important to keep in mind that not only sidesweeps from reflectors in the walls interior, but also interference from the air-rock boundary that is the face of the outcrop (wether its an actual geological outcrop, or a man made wall) can potentially interfere with the data. The PSF-based convolution method should therefore be tested on 3D models, and the results compared to 3D GPR-data, or other 3D modelling approaches like the Finite Difference method.

Chapter 5

Conclusion

This study demonstrates the use of the PSF-based convolution modelling approach to model synthetic GPR data. The modelling itself was done using P-wave velocity and seismic scale frequencies as a stand in for EM-waves, but has validity on the basis that TE-waves and acoustic waves are equivalent in terms of reflection coefficients in their respective domains (Laurain and Lecomte, 2001). The method is shown to generate data with similar resolution to that of real data with an equal source pulse frequency. The method successfully generated synthetic PSDM GPR data, however further testing of this method is suggested. Further studies could include: 3D modelling, rock physics modelling (where other geophysical parameters are taken into account such as conductivity or water saturation), and a comparison to Finite Difference modelling.

```
% PNG2SEGY
%
% Conversion of PNG image to segy for input into SeisRox.
%
% Note: The test plot in the end will claim that the vertical scale is in
% seconds - just ignore.
%
% 9 February, 2016, Dani Schmid / later modified (Lecomte)/ later slightly modified
% block and property values automatically assigned according to grey value,
% noise model for input as R0 (with G = 0, etc.
% Check with Isabelle Lecomte if you have the latest or need another use
% The produced SEG-Y can then be imported into NORSAR Software Suite for use
% in SeisRoX (target models as grids/cubes).

% User input
fname       = 'model_name';   % figure name (NB! grey codes, 32-bit!)
x_max       = 1237;    % number of pixels as columns (horizontal axis)
mpvp        = 1;       % no need to change; not used.

% Add path to SeisLab
addpath('SeisLab 3.02/S4M/Geophysics_3.0');

% Setup SeisLab presets
presets;
global S4M;

% Read image
[A,map]           = imread([fname, '.png']);
imshow(A,map);
colorbar;

A = squeeze(A(:,:,1));


% T1=50 Uncomment to set treshold for model assignment above or below pixel
% number T1
% T2=200 Uncomment to set treshold for model assignment above or below
```

```
% greyscale color code T2. Uncomment, the T1 and T2 lines below as well.

%% DATA decomposition
[n m] = size(A);
block = zeros(n,m);
vp = zeros(n,m); % NB! in km/s (NORSAR default unit)
vs = zeros(n,m); % NB! in km/s (NORSAR default unit)
rho = zeros(n,m); % NB! in kg/dm3 or equiv. (NORSAR default unit)
noise = zeros(n,m); % white noise
for i = 1:n
for j = 1:m
if A(i,j) == 111   % facies 1
block(i,j) = 1. ;
vp(i,j) = 0.95 ;
elseif A(i,j) == 46 % facies 2
block(i,j) = 2. ;
vp(i,j) = 0.85 ;
elseif A(i,j) == 164 % facies 3
block(i,j) = 3. ;
vp(i,j) = 1.0 ;
%        elseif A(i,j) == 192 & T2>256 % facies 4
%             block(i,j) = 4. ;
%             vp(i,j) = 3.0 ;
%         elseif A(i,j) > T1 % facies 5
%             block(i,j) = 5. ;
%             vp(i,j) = 0.90 ;
%         elseif A(i,j) <= T1 % facies 6
%             block(i,j) = 1. ;
%             vp(i,j) = 0.95 ;
else
block(i,j) = 2. ; % NB! in case of holes in model
vp(i,j) = 1.0 ;
end
vs(i,j) = 0; % constant Vs=0 for GPR models
rho(i,j) = 1; % constant density for GPR models
end
% create white noise grid with same size (number of pixels vertically)
cn = dsp.ColoredNoise('Color','white','SamplesPerFrame',m); %% colored noise functi
```

```
x = cn();
noise(i,:) = x /20.; %(NB! average noise 1, but reduced by 20. here)
clear('cn','x')
end

% Trace of seismic line
X           = linspace(0, x_max, size(A,2));
Y           = zeros(size(X));

% Create data structure - block
seis_fold.type              = 'seismic';
seis_fold.tag               = 'unspecified';
seis_fold.name              = fname;
seis_fold.line_number       = 1;
seis_fold.reel_number       = 1;
seis_fold.traces_per_record = size(A,2);
seis_fold.aux_per_record  = size(A,2);
seis_fold.cdp_fold          = 1;
seis_fold.first             = 0;
seis_fold.last              = size(A,1)-1;
seis_fold.step              = mpvp;
seis_fold.units             = 'm';
seis_fold.traces            = block;
seis_fold.null              = [];
seis_fold.header_info       = {...
'sou_x'         'm'      'X coordinate of source'
'sou_y'         'm'      'Y coordinate of source'
'rec_x'         'm'      'X coordinate of receiver'
'rec_y'         'm'      'Y coordinate of receiver'};
seis_fold.headers           = [X; Y; X; Y];
seis_fold.fp_format_of_segy_file    = 'ibm';

% Write segy
write_segy_file(seis_fold, [fname, '_block.sgy']);

% Read
seis_read = read_segy_file( [fname, '_block.sgy']);
```

```
% Plot
s_cplot(seis_read, {'colormap','jet'},{'title','Block #'},{'time_lines',}, {'limits
c = colorbar;
c.Label.String = '#';

% Create data structure - vp
seis_fold.type              = 'seismic';
seis_fold.tag               = 'unspecified';
seis_fold.name              = fname;
seis_fold.line_number       = 1;
seis_fold.reel_number       = 1;
seis_fold.traces_per_record = size(A,2);
seis_fold.aux_per_record  = size(A,2);
seis_fold.cdp_fold          = 1;
seis_fold.first             = 0;
seis_fold.last              = size(A,1)-1;
seis_fold.step              = mpvp;
seis_fold.units             = 'm';
seis_fold.traces            = vp;
seis_fold.null              = [];
seis_fold.header_info       = {...
'sou_x'         'm'      'X coordinate of source'
'sou_y'         'm'      'Y coordinate of source'
'rec_x'         'm'      'X coordinate of receiver'
'rec_y'         'm'      'Y coordinate of receiver'};
seis_fold.headers           = [X; Y; X; Y];
seis_fold.fp_format_of_segy_file    = 'ibm';

% Write segy
write_segy_file(seis_fold, [fname, '_vp.sgy']);

% Read
seis_read = read_segy_file( [fname, '_vp.sgy']);

% Plot
s_cplot(seis_read, {'colormap','jet'},{'title','Vp (km/s)'},{'time_lines',}, {'limi
c = colorbar;
c.Label.String = 'Vp (km/s)';
```

```
% Create data structure - vs
seis_fold.type              = 'seismic';
seis_fold.tag               = 'unspecified';
seis_fold.name              = fname;
seis_fold.line_number       = 1;
seis_fold.reel_number       = 1;
seis_fold.traces_per_record = size(A,2);
seis_fold.aux_per_record  = size(A,2);
seis_fold.cdp_fold          = 1;
seis_fold.first             = 0;
seis_fold.last              = size(A,1)-1;
seis_fold.step              = mpvp;
seis_fold.units             = 'm';
seis_fold.traces            = vs;
seis_fold.null              = [];
seis_fold.header_info       = {...
'sou_x'         'm'      'X coordinate of source'
'sou_y'         'm'      'Y coordinate of source'
'rec_x'         'm'      'X coordinate of receiver'
'rec_y'         'm'      'Y coordinate of receiver'};
seis_fold.headers           = [X; Y; X; Y];
seis_fold.fp_format_of_segy_file    = 'ibm';

% Write segy
write_segy_file(seis_fold, [fname, '_vs.sgy']);

% Read
seis_read = read_segy_file( [fname, '_vs.sgy']);

% Plot
s_cplot(seis_read, {'colormap','jet'},{'title','Vs (km/s)'},{'time_lines',}, {'limi
c = colorbar;
c.Label.String = 'Vs (km/s)';

% Create data structure - rho
seis_fold.type              = 'seismic';
seis_fold.tag               = 'unspecified';
```

```
seis_fold.name              = fname;
seis_fold.line_number       = 1;
seis_fold.reel_number       = 1;
seis_fold.traces_per_record = size(A,2);
seis_fold.aux_per_record  = size(A,2);
seis_fold.cdp_fold          = 1;
seis_fold.first             = 0;
seis_fold.last              = size(A,1)-1;
seis_fold.step              = mpvp;
seis_fold.units             = 'm';
seis_fold.traces            = rho;
seis_fold.null              = [];
seis_fold.header_info       = {...
'sou_x'         'm'      'X coordinate of source'
'sou_y'         'm'      'Y coordinate of source'
'rec_x'         'm'      'X coordinate of receiver'
'rec_y'         'm'      'Y coordinate of receiver'};
seis_fold.headers           = [X; Y; X; Y];
seis_fold.fp_format_of_segy_file    = 'ibm';

% Write segy
write_segy_file(seis_fold, [fname, '_rho.sgy']);

% Read
seis_read = read_segy_file( [fname, '_rho.sgy']);

% Plot
s_cplot(seis_read, {'colormap','jet'},{'title','Density (kg/dm3)'},{'time_lines',},
c = colorbar;
c.Label.String = 'Rho (kg/dm3)';

% Create data structure - noise
seis_fold.type              = 'seismic';
seis_fold.tag               = 'unspecified';
seis_fold.name              = fname;
seis_fold.line_number       = 1;
seis_fold.reel_number       = 1;
seis_fold.traces_per_record = size(A,2);
```

```
seis_fold.aux_per_record  = size(A,2);
seis_fold.cdp_fold          = 1;
seis_fold.first             = 0;
seis_fold.last              = size(A,1)-1;
seis_fold.step              = mpvp;
seis_fold.units             = 'm';
seis_fold.traces            = noise;
seis_fold.null              = [];
seis_fold.header_info       = {...
'sou_x'         'm'      'X coordinate of source'
'sou_y'         'm'      'Y coordinate of source'
'rec_x'         'm'      'X coordinate of receiver'
'rec_y'         'm'      'Y coordinate of receiver'};
seis_fold.headers           = [X; Y; X; Y];
seis_fold.fp_format_of_segy_file    = 'ibm';

% Write segy
write_segy_file(seis_fold, [fname, '_noise.sgy']);

% Read
seis_read = read_segy_file( [fname, '_noise.sgy']);

% Plot
s_cplot(seis_read, {'colormap','jet'},{'title','White noise'},{'time_lines',}, {'li
c = colorbar;
c.Label.String = 'Noise value';
```

Bibliography

Ai, Songtao et al. (Feb. 2014). "Topography, ice thickness and ice volume of the glacier Pedersenbreen in Svalbard, using GPR and GPS". In: *Polar Research* 33. DOI: 10.3402/polar.v33.18533.

Andersen, Ingvild G. (2020). "Effects of geophysical parameters on the seismic expression of the Maghlaq Fault, Malta: insights from outcrop-based 2D seismic modeling". MA thesis. University of Bergen.

Annan, A.P. (2009). "Chapter 1 - Electromagnetic Principles of Ground Penetrating Radar". In: *Ground Penetrating Radar Theory and Applications*. Ed. by Harry M. Jol. Amsterdam: Elsevier, pp. 1 –40. ISBN: 978-0-444-53348-7. DOI: https://doi.org/10.1016/B978-0-444-53348-7.00001-6.

Apel, Derek and V. Dezelic (Dec. 2005). "Evaluation of high frequency ground penetrating radar (GPR) in mapping strata of dolomite and limestone rocks for ripping technique". In: *International Journal of Surface Mining, Reclamation and Environment* 19, pp. 260–275. DOI: 10.1080/13895260500275418.

Cassidy, Nigel J. (2009). "Chapter 2 - Electrical and Magnetic Properties of Rocks, Soils and Fluids". In: *Ground Penetrating Radar Theory and Applications*. Ed. by Harry M. Jol. Amsterdam: Elsevier, pp. 41 –72. ISBN: 978-0-444-53348-7. DOI: https://doi.org/10.1016/B978-0-444-53348-7.00002-8.

Dalsegg, Einar, Harald Elvebakk, and Jan Steinar Rønning (2005). *2D resistivitet og georadarmålinger Ebbadalen og Wordiekammen, Billefjorden, Svalbard*. Tech. rep. 2004.058. Geological Survey of Norway.

Eide, Christian Haug et al. (2018). "Seismic interpretation of sill complexes in sedimentary basins: implications for the sub-sill imaging problem". In: *Journal of the Geological Society* 175.2, pp. 193–209. ISSN: 0016-7649. DOI: 10.1144/jgs2017-096.

Goodman, Dean (Feb. 1994). "Ground-Penetrating Radar Simulation in Engineering and Archaeology". In: *Geophysics* 59, pp. 224–232. DOI: 10.1190/1.1443584.

Guéguen, Y. and V. Palciauskas (1994). *Introduction to the Physics of Rocks*. Princeton University Press. ISBN: 9780691034522.

Hagen, Heming (2012). *Tilstandsvurdering av Lyse klosterium, Bergen Kommune*.

Hagevold, Sondre (2019). "From outcrop to synthetic seismic: 2D and 3D modelling of igneous intrusions at Botneheia, central Spitsbergen". MA thesis. University of Bergen.

Janocha, Julian et al. (2020). "Seeing beyond the outcrop: Integration of ground-penetrating radar with digital outcrop models of a paleokarst system". In: *Marine and Petroleum Geology*, p. 104833. ISSN: 0264-8172. DOI: https://doi.org/10.1016/j.marpetgeo.2020.104833.

Laurain, R. and I. Lecomte (2001). "Elastic/Electromagnetic Wave Propagation - Equivalences and 2D Modelling of GPR". In: cp-15-00198. ISSN: 2214-4609. DOI: https://doi.org/10.3997/2214-4609-pdb.15.P142.

Ryan, Harold (Sept. 1994). "Ricker, Ormsby, Klander, Butterworth – A Choice of Wavelets". In: *Recorder CSEG* 19.

Tveranger, Jan et al. (Jan. 2020). "Permo-Carboniferous paleokarst structures at Wordiekammen, central Svalbard". In.